Journal of Geophysical Research: Oceans

RESEARCH ARTICLE
10.1029/2018JC014162

Structure and Transport of the North Atlantic Current in the Eastern Subpolar Gyre From Sustained Glider Observations

L. Houpert[1], M. E. Inall[1], E. Dumont[1], S. Gary[1], C. Johnson[1], M. Porter[1], W. E. Johns[2], and S. A. Cunningham[1]

[1]Scottish Association for Marine Science, Oban, UK, [2]Rosenstiel School of Marine and Atmospheric Science, Miami, FL, USA

Key Points:
- Two branches of the North Atlantic Current (named the Hatton Bank Jet and the Rockall Bank Jet) are revealed by repeated glider sections
- Around 6.3+/-2.1 Sv is carried by the Hatton Bank Jet in summer, about 40% of the upper-ocean transport by the North Atlantic Current across 59.5N
- Thirty percent of the Hatton Bank Jet transport is due to the vertical geostrophic shear while the Hatton-Rockall Basin currents are mostly barotropic

Correspondence to:
L. Houpert,
loic@lhoupert.fr

Citation:
Houpert, L., Inall, M. E., Dumont, E., Gary, S., Johnson, C., Porter, M., et al. (2018). Structure and transport of the north atlantic current in the Eastern Subpolar Gyre from sustained glider observations. *Journal of Geophysical Research: Oceans*, *123*, 6019–6038. https://doi.org/10.1029/2018JC014162

Received 8 MAY 2018
Accepted 13 JUL 2018
Accepted article online 23 JUL 2018
Published online 29 AUG 2018

Abstract Repeat glider sections obtained during 2014–2016, as part of the Overturning in the Subpolar North Atlantic Program, are used to quantify the circulation and transport of North Atlantic Current (NAC) branches over the Rockall Plateau. Using 16 glider sections collected along 58°N and between 21°W and 15°W, absolute geostrophic velocities are calculated, and subsequently the horizontal and vertical structure of the transport are characterized. The annual mean northward transport (± standard deviation) is 5.1 ± 3.2 Sv over the Rockall Plateau. During summer (May to October), the mean northward transport is stronger and reaches 6.7 ± 2.6 Sv. This accounts for 43% of the total NAC transport of upper-ocean waters (σ_O < 27.55 kg/m^3) estimated by Sarafanov et al. (2012, https://doi.org/10.1029/2011JC007572) along 59.5°N, between the Reykjanes Ridge and Scotland. Two quasi-permanent northward flowing branches of the NAC are identified: (i) the Hatton Bank Jet (6.3 ± 2.1 Sv) over the eastern flank of the Iceland Basin (20.5°W to 18.5°W) and (ii) the Rockall Bank Jet (1.5 ± 0.7 Sv) over the eastern flank of the Hatton-Rockall Basin (16°W to 15°W). Transport associated with the Rockall Bank Jet is mostly depth independent during summer, while 30% of the Hatton Bank Jet transport is due to vertical geostrophic shear. Uncertainties are estimated for each individual glider section using a Monte Carlo approach, and mean uncertainties of the absolute transport are less than 0.5 Sv. Although comparisons with altimetry-based estimates indicate similar large-scale circulation patterns, altimetry data do not resolve small mesoscale current bands in the Hatton-Rockall Basin which are strongly needed for the right transport estimates.

Plain Language Summary There is mounting evidence that heat and freshwater transported by the North Atlantic Current (eastward extension of the Gulf Stream) heavily influences European and global climate. To adequately measure this current and understand its dynamics, underwater gliders navigate over the Rockall Plateau, a remote region of the North Atlantic located more than 400 km off Scotland. These robots collect data up to a kilometer beneath the ocean's surface and, due to their low energy consumption, can operate over thousands of kilometers for months at a time. This study analyzes 2 years of continuous ocean glider measurements in the North Atlantic and reveals two branches of the North Atlantic Current over the Rockall Plateau that we named the Hatton Bank Jet and the Rockall Bank Jet. For the first time, the monthly variability of these currents was characterized (speed and horizontal/vertical extension). These branches carry a significant portion of the upper-ocean waters transported by the North Atlantic Current (40%). This work highlights the importance of using autonomous underwater vehicles as part of an ocean observatory. In addition to monitoring the *state* of the North Atlantic Ocean, these underwater robots help us understand its dynamics, which impacts the European and global climate.

1. Introduction

The Atlantic Meridional Overturning Circulation (AMOC) is characterized by a northward flux of warm upper-ocean waters and a compensating southward flux of cool deep waters, playing a fundamental role in the global climate system and its variability (Buckley & Marshall, 2016; Intergovernmental Panel on Climate Change, 2014). Heat advected northward as part of the upper AMOC limb plays an important role in moderating western European climate (Rhines et al., 2008) and is linked to the decline of Arctic sea ice (Serreze et al., 2007) and mass loss from the Greenland Ice Sheet (Straneo et al., 2010). In addition, variations in AMOC strength are believed to influence North Atlantic sea surface temperatures, with potential impacts on rainfall

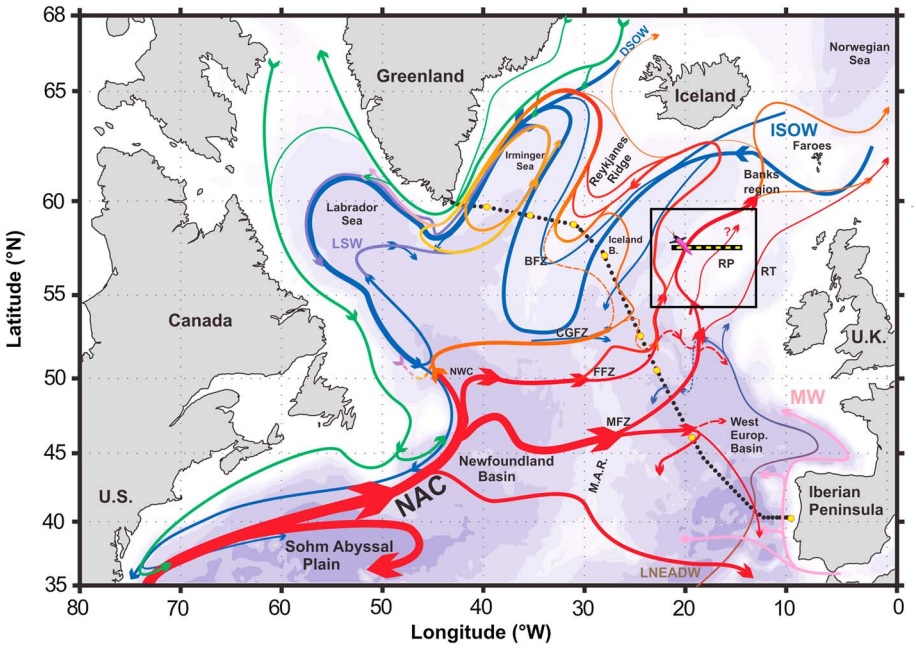

Figure 1. Schematic view of the main circulation pathways in the Subpolar North Atlantic Gyre adapted from Daniault et al. (2016), showing the relatively warm surface and intermediate water and the cold deep waters. The nominal UK-OSNAP glider section is shown as a yellow dashed line (from 21°W to 15°W). Absolute geostrophic and bathymetry details in the box area are shown in Figure 2. NAC = North Atlantic Current; NWC = Northwest Corner; BFZ = Bigth Fracture Zone; CGFZ = Charlie-Gibbs Fracture Zone; FFZ = Faraday Fracture Zone; MFZ = Maxwell Fracture Zone; MAR = Mid-Atlantic Ridge; RP = Rockall Plateau; RT = Rockall Trough; ISOW = Iceland-Scotland Overflow Water; DSOW = Denmark Strait Overflow Water; MW = Mediterranean Water; LNEADW = Lower Northeast Atlantic Deep Water; LSW = Labrador Sea Water; UK-OSNAP = UK-Overturning in the Subpolar North Atlantic Program.

over the African Sahel, Atlantic hurricane activity, and summer climate over Europe and North America (Smith et al. 2010; Sutton ; 2005; Zhang and Delworth ; 2006).

Subtropical waters enter the North Atlantic Subpolar Gyre through the upper part of the North Atlantic Current (NAC, Figure 1), strongly constrained by bathymetry (Daniault et al., 2016). About 60% (12.7 Sv) of the waters carried in the upper limb of the AMOC ($\sigma_0 < 27.55$) by the NAC and the Irminger Current are estimated to recirculate in the Subpolar Gyre; 10.2 Sv of this recirculating water gains density and contributes to the lower limb of the AMOC, while 2.5 Sv exits the Irminger Sea in the Western Boundary Current in the upper limb (Sarafanov et al., 2012). The remaining 40% of upper-ocean water (between 7.5 and 8.5 Sv) is carried poleward by the NAC between Greenland and Scotland (Hansen et al. 2010; Rossby and Flagg; 2012), with the majority (90%) flowing east of Iceland. Although the amounts of warm upper-ocean waters recirculating and exiting the gyre are relatively well known, the energetic eddy field (Heywood et al., 1994) challenges the identification of an unequivocal relationship between the NAC branches in the eastern basin and those at the Mid-Atlantic Ridge (Daniault et al., 2016).

The Rockall Plateau (RP), also known as Rockall-Hatton Plateau, is characterized by a shallow topography and is formed by the Hatton Bank (HB), the Hatton Rockall Basin (HRB), and the Rockall Bank (RB), as seen in Figures 1 and 2a. Weak stratification leads to a small radius of deformation (<10 km; Chelton et al., 1998), this radius of deformation, a characteristic scale of the mesoscale eddy field, requires an appropriate sampling strategy to resolve and adequately characterize the flow. All previous observations from research vessels in this region have a nominal station spacing too large (about 30–50 km; Bacon, 1997; Holliday et al., 2015; Sarafanov et al., 2012) to correctly resolve the mesoscale field over the RP.

Inaccuracies in knowledge of the geoid in this region (Chafik et al., 2014) also lead to uncertainties in altimetry-derived estimates of the circulation and its variability. To resolve the net circulation over the RP, a glider endurance line was designed from the RB to a deep mooring located in the Iceland Basin at 21°W, as part of the Overturning in the Subpolar North Atlantic Program (OSNAP; Lozier et al., 2017; Figure 2a). OSNAP

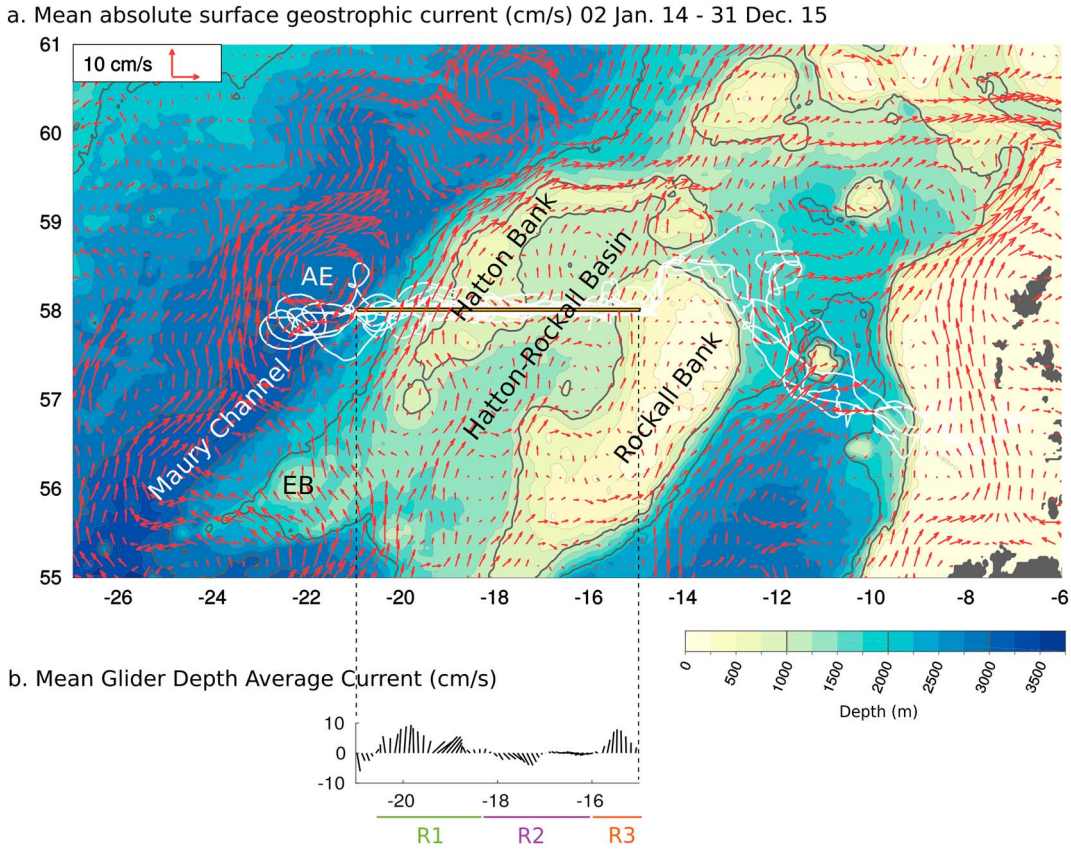

Figure 2. (a) Two-year mean surface absolute geostrophic current (arrows) for the 2014–2015 period, with the glider mission tracks (white) and bathymetry contours in color from GEBCO bathymetry (http://www.gebco.net/). AE = Anticyclonic Eddy; EB = Edoras Bank; GEBCO = General Bathymetric Chart of the Oceans. (b) Mean glider depth average current (m/s) from 21°W to 14.5°W, with the limits of the three regions mentioned in the manuscript.

is a transatlantic observing system consisting of multiple mooring arrays supplemented by the repeat glider section across the RP.

We present data from 16 glider sections collected along 58°N, between 21°W and 15°W from July 2014 to August 2016. Glider and altimetry data are presented in section 2. In section 3, we introduce the methods used to calculate absolute geostrophic velocity from glider measurements. In section 4, we present and discuss our results on the spatial structure of the flow and associated transport over the RP and compare them with altimetry-based estimates. Section 5 summarizes the principal findings of this study.

2. Data

2.1. Glider Sections

The gliders used in the present study perform saw-tooth trajectories from the surface to maximum depths of 1,000 m. With a pitch angle (of above 25°) much larger than isopycnal slopes, glider dives and climbs can be considered as quasi-vertical profiles. Using a ballast pump and wings, they achieve vertical speeds of 10–20 cm/s and forward speeds of 20–40 cm/s. They are designed for missions of several thousand kilometers and durations of many months, well suited to observe ocean boundary currents (Lee & Rudnick, 2018; Liblik et al., 2016; Rudnick, 2016; Testor et al., 2010). Consecutive surfacings are separated by about 2–6 km and 4–6 hr when diving to 1-km depth (see Table 1, for the OSNAP mission statistics). Over each dive cycle, the depth-average current (DAC) can be derived from the Seaglider dead reckoning navigation and GPS fixes at surface. The DAC accuracy is within 1 cm/s for a glider with stable flight characteristics (Eriksen et al., 2001; Todd et al., 2011). Owing to their direct DAC measurement, gliders produce absolutely referenced geostrophic velocity that can be used to accurately quantify current transports (Eriksen et al., 2001; Rudnick & Cole, 2011).

Table 1
Summary of Glider Mission and Sampling on the OSNAP Glider Endurance Line (West of 15°W), Including Dates, Mean and Standard Deviation of Dive Displacement and Duration, and Number of Quality-Controlled Temperature and Salinity Profiles (Dive+Climb)

Occupation dates	Δx (km)	Δt (hr)	T profiles	S profiles
16 Jul 2014 to 22 Nov 2014	2.70 ± 1.22	4.33 ± 1.47	658	518
24 Nov 2014 to 21 Feb 2015	2.95 ± 1.65	4.60 ± 1.43	434	432
31 Mar 2015 to 24 Jun 2015	3.58 ± 2.24	5.09 ± 1.08	399	398
10 Jun 2015 to 28 Nov 2015	3.26 ± 1.65	4.93 ± 0.86	804	787
22 Mar 2016 to 22 Jun 2016	3.49 ± 1.64	4.83 ± 0.81	431	431

Note. OSNAP = Overturning in the Subpolar North Atlantic Program.

From July 2014 to July 2016, five gliders were deployed as part of the UK-OSNAP glider program. Sixteen sections, one section every 1–2 months, were completed over the RP (Figure 2a). In total, 6,000 temperature and salinity profiles were acquired west of 15°W. To reduce energy demand, the conductivity-temperature-depth packages on Seagliders are unpumped and the cell is flushed by flow past the glider. Glider speed changes slowly, providing a nearly steady flushing rate of the conductivity cell, just as provided conventionally by a pump (Eriksen et al., 2001). Automatic quality control protocols are applied on the raw temperature/salinity data: spikes are removed; and the thermistor lag and thermal-inertia of the conductivity sensors are corrected by the Seaglider basestation v2.09 (University of Washington, 2016). Suspicious data points are identified by comparing to a reference database (World Ocean Data Base ; Boyer et al., 2013) and OSNAP cruise and mooring data (Lozier et al., 2017); 5.7% of salinity data and 2.2% of temperature data over RP are flagged as bad and are not used in this work.

The measurement accuracies of the Conductivity-Temperature (CT) sensors are given by the manufacturer Sea-Bird Scientific: 0.002 °C for temperature and 0.005 S/m for conductivity (equivalent to an accuracy of 0.05 in salinity for standard conditions: $T = 15$ °C, $S = 35$, $P = 0$ dbar). Point-by-point comparisons are made between the Seaglider conductivity-temperature-depth and calibrated SBE37 (microcat) T/S sensors on OSNAP mooring M4 at 58°N, 21°W. We kept only the glider profiles performed near the mooring (<5 km). We found that the differences are lower than 0.26 °C in temperature and 0.03 in salinity. This difference in temperature can be explained by the high natural variability of the temperature at this location: although the temperature and salinity standard deviation in the top 1,000 m are the smallest at 900 m, the standard deviation of the temperature time series from the 900-m moored SBE37 is still relatively high (0.37 °C). Therefore, mooring data cannot be used for cross-calibration with the glider temperature measurements. The standard deviation of the salinity data at 900-m depth (0.03) has the same order of magnitude as the expected accuracy for the the salinity measurement, and therefore, the 900-m moored SBE37 can be used to assess the accuracy of the glider salinity data. We estimate, from the glider-mooring comparisons, that the salinity measurement accuracy is consistent with the accuracy provided by the manufacturer Sea-Bird Scientific.

The glider flight model influences estimates of vertical velocities, thermal-inertia in the CT system, and DAC. The internal flight model fit is improved by regressing variable buoyancy device and hydrodynamic parameters following the method used in Frajka-Williams et al. (2011), for each glider mission. Vertical velocities are derived from regressions from the difference between the predicted glider flight speed from the flight model and the observed glider vertical velocity from first difference pressure data. Applying regressions for each glider mission, the root-mean-square difference of the vertical velocity estimated by the Seaglider is less than 2.0 cm/s (from 0.8 to 1.9 cm/s depending on the particular glider mission), indicating an optimized flight model fit.

2.2. Altimetry

We use delayed time data from the SSALTO/DUACS (Data Unification and Altimeter Combination System) system (Pujol et al., 2016): daily global absolute sea-surface dynamic topography, absolute geostrophic velocity and geostrophic velocity anomalies (spatial resolution of 0.25°). These are distributed through The Copernicus Marine and Environment Monitoring Service (http://marine.copernicus.eu/documents/QUID/CMEMS-SL-QUID-008-032-051.pdf). This system consists of a homogeneous, intercalibrated time series of sea level anomaly and mean sea level anomaly (combining data from 13 missions). Absolute sea surface dynamic topography is the sum of sea level anomaly and a mean dynamic topography, both referenced over

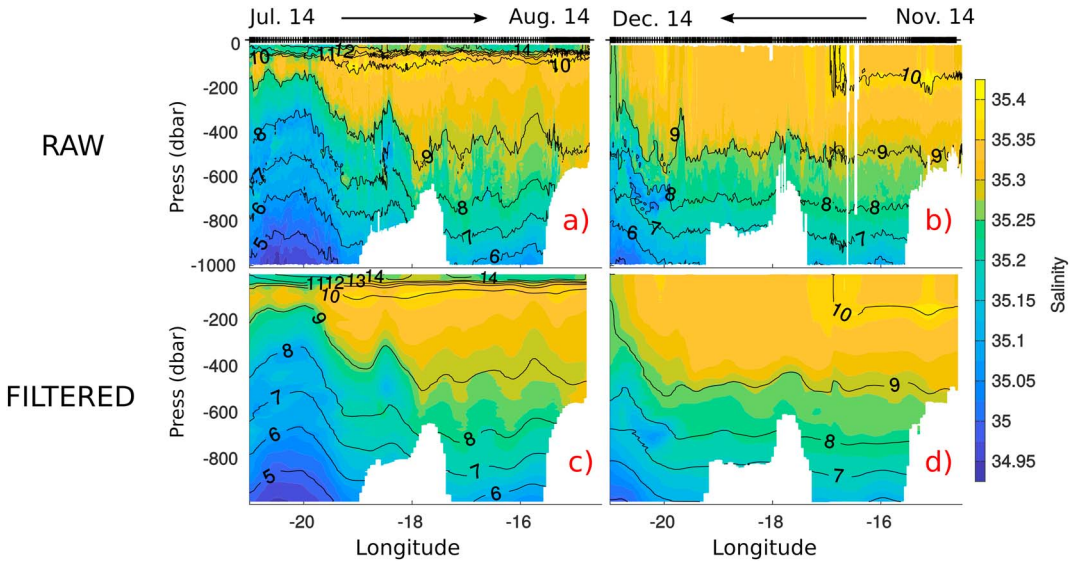

Figure 3. Individual glider sections observed from July to August 2014 (a) and from November to December 2014 (b), showing salinity with potential temperature contour binned in 2-m vertical bins; (c, d) same data filtered using a Gaussian moving average of 8-km variance corresponding to a full width at half maximum of 18.8 km.

a 20-year period (1993–2012). The combination of altimetric data with other data sets (e.g., in situ, gravimetric, and satellites) is used to determine the geoid at a horizontal resolution of 125 km and compute the mean dynamic topography (MDT-CNRS-CLS2013). Multivariate objective analysis (including wind and in situ data) is used to improve the large-scale solution, resulting in a final gridded horizontal resolution of 0.25°. The data are analyzed from 1 January 2014 to 1 January 2016. We used the gridded surface geostrophic anomalies derived from the Sea Level Anomaly (SLA) gradients to calculate the eddy kinetic energy (EKE). The surface EKE is calculated as one half of the sum of the squared eddy velocity components.

3. Absolute Geostrophic Current and Transport From Gliders

From glider density sections and DAC, one can calculate the cross-track absolute geostrophic current. As in Bosse et al. (2015), we filter the density sections and DAC time series by using a Gaussian moving average in order to filter out small-scale isopycnal oscillations mostly due to aliased sampling of high frequency internal waves (Figures 3a and 3b). The full width at half maximum (18.8 km, corresponding to a Gaussian standard deviation of 8 km) is chosen to be of the order of the deformation radius (<10 km; Chelton et al., 1998).

Following Høydalsvik et al. (2013), the cross-track geostrophic vertical shear is computed by integrating the thermal wind balance (equation (1):

$$\rho_0 f \frac{\partial v_n}{\partial z} = -g \frac{\partial \rho}{\partial s} \tag{1}$$

where s is the along-section coordinate, z is the vertical coordinate, $v_n(z)$ is the velocity normal to the section, f is the Coriolis parameter, g is the acceleration of gravity, ρ is the density, and ρ_0 is a reference density (1,025 kg/m^3).

By integrating equation (1) from the maximum depth H to the depth z, we obtain equation (2):

$$v_n(z) = v_n(-H) \underbrace{- \frac{g}{\rho_0 f} \int_{-H}^{z} \frac{\partial \rho}{\partial s} \mathrm{d}z}_{v_{BC}(z)} \tag{2}$$

where $v_n(-H)$ is the velocity at the maximum diving depth and $v_{BC}(z)$ is the baroclinic component of the geostrophic velocity relative to depth H.

The vertically integrated Ekman current that the glider experiences during a dive can be estimated by dividing the local Ekman transport by the diving depth (always larger than the Ekman penetration depth in this area). Ekman transport is calculated every 6 hr on 0.5° longitude grid at 58°N, using ERA-Interim 10-m winds (https://www.ecmwf.int) for the 2014–2015 period in combination with a bulk formula for the wind stress,

Table 2
Transport Uncertainty (Sv) for Each Individual Glider Section (Numbered From S1 to S20), Defined as 1 Standard Deviation Between the 100 Ensemble Members of the Monte Carlo Approach Detailed in Appendix A

Section	Region R1	Region R2	Region R3	All
S1	0.07	0.04	0.02	0.11
S2	0.14	N.A.	0.02	N.A.
S3	N.A.	N.A.	0.04	N.A.
S4	N.A.	0.05	0.09	N.A.
S5	N.A.	0.04	0.02	N.A.
S6	0.08	0.08	0.04	0.16
S7	0.05	0.09	0.02	0.12
S8	0.04	0.11	0.04	0.13
S12	0.37	0.38	0.30	0.69
S13	0.24	0.23	0.43	0.62
S14	0.17	0.32	0.27	0.47
S16	N.A.	0.33	0.06	N.A.
S17	N.A.	0.22	0.14	N.A.
S18	0.41	0.45	0.27	0.73
S19	0.43	0.43	0.10	0.50
S20	0.41	0.96	0.10	1.12
Mean	0.22	0.27	0.12	0.46
σ	0.16	0.25	0.13	0.34

Note. The mean uncertainty calculated over all sections and the standard deviation are also indicated.

with a drag coefficient defined as in Trenberth et al. (1990). Over the 2014–2015 period and from 21°W to 15°W, the 6-hourly DAC Ekman values vary from −1.7 to 0.6 cm/s. The mean (±1 standard deviation) is −0.06 cm/s (±0.17 cm/s), which is 1 to 2 orders of magnitude smaller than the observed mean DAC along the section (V_{DAC}). Because of their small mean contribution, no Ekman corrections are applied to the DAC.

We estimate the dive-by-dive average tidal current to be of order 1 cm/s by using a 1/12° Atlantic tidal prediction model with the Matlab toolbox Tidal Model Driver (Egbert & Erofeeva, 2002). This tidal contribution is 1 order of magnitude less than the DAC associated with the mesoscale currents we are interested in. The mean displacement speed of the glider is 17.5 km/day (Table 1): Therefore, the spatial Gaussian filter applied with a half maximum of 18.8 km is equivalent to a temporal filter with half maximum of 1 day. The Gaussian window effectively low-pass filters the data (Bosse et al., 2015; Pelland et al., 2013; Todd et al., 2009); thus, the small tidal contribution is mostly removed by the filtering of V_{DAC}. The effectiveness of this method is confirmed by comparing to data initially low-pass filtered with a 48-hr Butterworth filter (tide removal filter). Results showed that the final data sets are identical when applying the Gaussian moving average on raw data or on low-pass filtered data.

We can then consider that the vertical integral of $v_n(z)$ over the depth of the dive (H) is equal to the DAC (V_{DAC}, equation (3):

$$V_{DAC} = \frac{1}{H}\int_{-H}^{0} v_n(z)\,dz \tag{3}$$

By integrating equation (2) over the water column, and using equation (3), we obtain the velocity at the maximum diving depth $v_n(-H)$ (equation (4). Then $v_n(z)$ can then be estimated for each depth z by using equation (4) in equation (2).

$$\begin{aligned} V_{DAC} &= v_n(-H) + \frac{1}{H}\int_{-H}^{0} v_{BC}(z)\,dz \\ v_n(-H) &= V_{DAC} - \frac{1}{H}\int_{-H}^{0} v_{BC}(z)\,dz \end{aligned} \tag{4}$$

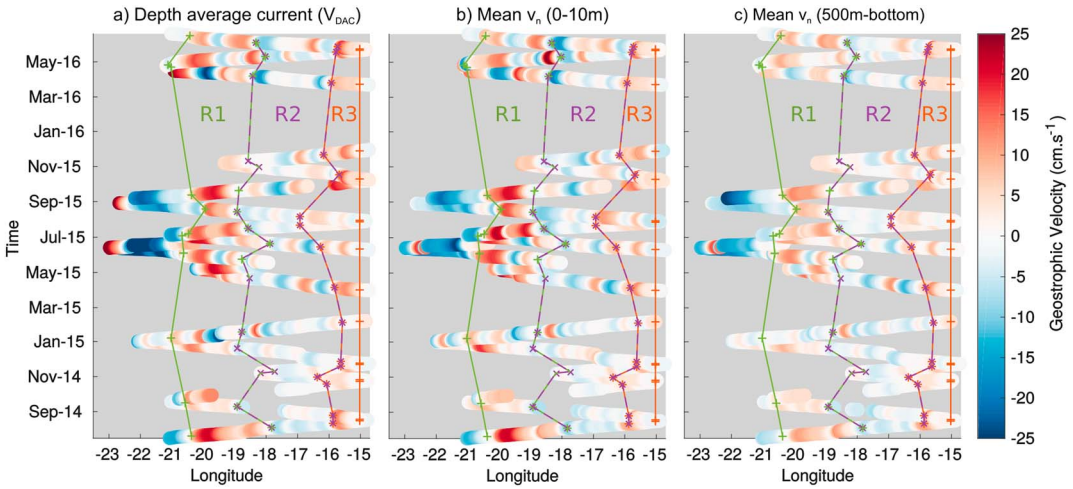

Figure 4. (a) Time series of the meridional component of the depth average current, and time series of the average absolute meridional geostrophic current for (b) the near-surface layer (0–10 m) and (c) below the seasonal pycnocline (500-m bottom). The western and eastern limits of the three regions mentioned in the manuscript are shown for each section: Region R1 (the Hatton Bank Jet) in green, Region R2 in purple, and Region R3 (the Rockall Bank Jet) in orange.

In summary, absolute geostrophic velocities are obtained by vertically integrating the thermal wind balance (equation (2) along the glider path from the surface to the maximum diving depth. The reference velocity at the maximum diving depth is deduced from the section-normal component of the DAC (equation (4)).

The along-path geostrophic velocity fields are then projected onto a regular longitudinal grid along 58°N. For each glider section, all the nearby velocity profiles are binned onto a 0.05° regular longitude grid, and for each bin, we use the velocity profile with the closest f/h value compared to the f/h bin value (f is the Coriolis parameter and h the water depth).

Meridional absolute geostrophic transport (ϕ_{abs}, equation (5) is calculated by integrating absolute geostrophic velocity along the glider section, from the surface to 1,000 m, or to the bottom where the depth is less than 1,000 m.

$$\phi_{abs} = \iint_{section} v_n(z)\mathrm{d}x\mathrm{d}z \tag{5}$$

The uncertainty in transport is estimated for each section, using a Monte Carlo approach. The density field and reference velocities are perturbed to take into account uncertainties in (i) the temperature-salinity data and (ii) the DAC estimated from the glider (see details in Appendix A). Each glider section is described by an ensemble of 100 randomly perturbed sections. The ϕ_{abs} is then defined for each section as the mean of the 100 ensemble members, and the uncertainty on ϕ_{abs} is defined as 1 standard deviation between the 100 ensemble members (Table 2). The mean uncertainty of the absolute transport on the whole section (from 20.5°W to 15°W) is calculated by averaging uncertainty for all individual sections and is equal to 0.46 Sv (Table 2).

4. Results

4.1. Spatial and Temporal Variability of the North Atlantic Current Branches Over the Rockall-Hatton Plateau

To define the spatial scales of the main currents, we first look at the mean DAC from the repeated glider sections, shown in Figure 2b. Three different flows can be distinguished: a northward flow extending from 20.5°W to 18.5°W (on the Eastern flank of the Iceland Basin, *Region R1*), a southward flow extending from 18.5°W to 16.0°W (on the Western flank of the HRB, *Region R2*), and a northward flow between 16.0°W, 15.0°W (on the Eastern flank of the HRB, *Region R3*).

The position and the zonal width of these three currents varies in time (Figure 4a). We define the western and eastern limits of the northward flowing currents over Region R1 and the western limit over Region R3, as the zero-crossing locations of the meridional component of the DAC (Figure 4a). The eastern limit of the northward flow in Region R3 is set to the easternmost point of the section, on Rockall Bank at 15°W. The

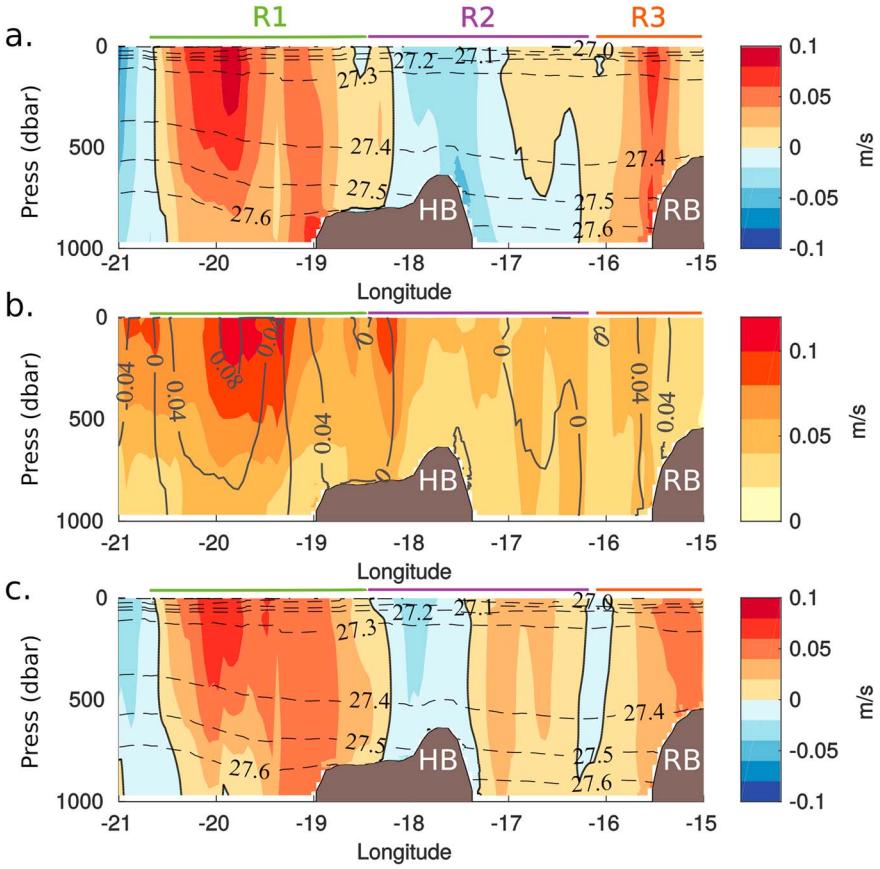

Figure 5. (a) Mean absolute meridional geostrophic velocity (m/s) referenced to glider depth-average current. (b) Standard deviation of the absolute meridional geostophic velocity between glider sections. (c) Mean absolute meridional geostrophic velocity referenced to surface absolute geostrophic current from altimetry (for the observational glider period 2014–2016). Dashed lines correspond to potential density contours. The solid black contour lines are the 0-m/s geostrophic velocity contours.. The mean zonal widths of the three regions R1, R2, and R3 are shown on top of the section (R1: 20.5°W/18.5°W; R2: 18.5°W/16.0°W; and R3: 16.0°W/15.0°W).

horizontal extent of the southward flow in Region R2 is defined as the area between these two northward flows. The mean western and eastern limits of all individual sections are similar to those on the mean DAC time series (Figure 2b).

Sixteen glider sections spanned the entire region of study from 15°W to 21°W. The mean absolute meridional geostrophic velocities are derived from all sections (Figure 5a). Northward velocities (positive values) extend over the top 1,000 m of the water column in Region R1 and in Region R3. These two northward flows seem to be semipermanent branches that form part of the total NAC flow and are named hereafter the Hatton Bank Jet (Region R1) and the Rockall Bank Jet (Region R3). A southward flow is seen in between these two jets in Region R2.

The maximum mean northward geostrophic velocities are respectively 0.09 (core of R1) and 0.08 m/s (core of R3; Figure 5a), while the maximum geostrophic velocities measured during the observing period are respectively 0.25 (core of R1) and 0.22 m/s (core of R3). The variability of the current, shown by the standard deviation between sections (Figure 5b), is largest in the top 400 m west of 18°W (within R1). This higher variability may be due to the meandering of the Hatton Bank Jet and to the presence of two distinct cores which can be seen on the mean section as two local maxima centered on 19°W and 19.9°W (Figure 5). Two branches appear to form upstream at the entrance of the HRB, around 55°N/21°W: one branch enters the center of the HRB, while the other flows between Edoras Bank and HB (Figure 2a; see also Xu et al., 2015).

To examine the vertical structure and coherency of the flow, we show in Figure 4b the absolute geostrophic velocity near the surface and at depth. The near surface velocity (0–10 m) and the velocity below the seasonal

pycnocline (Figure 4c), averaged from 500 to 1,000 m (or to the bottom if shallower than 1,000 m), have a similar time and space variability, indicating that the flow is vertically coherent but surface intensified.

In Region R2, from 18.5°W to 16.0°W, the prevailing flow is southward (Figure 5a) with an intensity varying in time and space (Figure 4). The mean absolute geostrophic velocity is centered between 18°W and 17°W (Figure 5a), with a value of −0.05 m/s found at 770 m depth, on the Western flank of the HRB, at 17.5°W. During the period of observation, the minimum geostrophic velocity recorded was −0.20 m/s in April 2016 and localized in the surface layer (20 m) at 18.2°W.

Although the flow appears to be meandering (Figure 4), its mean position in each region seems to be associated with bathymetric features, particularly on steep slopes (Figure 5a):

- The Rockall Bank Jet in Region R3 (15.5°W) is centered on the 1,000 m contour, on a steep bathymetry change associated with the eastern flank of the HRB.
- The core of the southward flow in Region R2 (17.5°W) is centered on the 800-m contour, on the steep slope of the western flank of the HRB.
- The Hatton Bank Jet in Region R1 is divided into two cores, one associated with the steep western flank of the HB (19.0°W) and one centered on the 1,700-m isobath (19.9°W).

4.2. Meridional Absolute Geostrophic Transport

Meridional geostrophic velocity sections are integrated to provide absolute transport as a function of depth, density, and longitude (Figure 6). We choose to separate the 16 sections into two periods, distinguishing *winter* sections (November to April) when subpolar mode formation occurs, from the *summer* sections (May to October).

As a function of depth, the extrema of transport can be found in the top 200 m (Figures 6a and 6c). Two differences can be seen between the summer and the winter periods:

1. The southward transport in Region R2 seems to be approximately equal to the northward transport in Region R3 during summer, with transport per depth over the whole section approximately equal to the transport in Region R1. However, during winter the transport per depth over the whole section is 1.5 to 2 Sv lower than the transport per depth in Region R1 (Figure 6c), due to an increase in the southward transport in Region R2 and a decrease in the northward transport in Region R3 (Figures 6a and 6c).
2. The transport per depth during summer decreases with depth for Region R1 and Region R2, while during winter the transport per depth is more nearly constant from the surface to 600 m, corresponding to the depth attained by the mixed layer during winter (Lozier et al., 2017).

As a function of potential density, the extrema in transport are between 27.3 and 27.4 kg/m^3 (Figures 6b and 6d), corresponding to the density class of subpolar mode water over the RP (Brambilla & Talley, 2008). A main difference between summer and winter is the smaller transport of density <27.3 kg/m^3 in all regions during winter, which can be explained by the occurrence of subpolar mode water formation: The lighter water masses at the surface are transformed into denser intermediate mode water through winter buoyancy losses.

A clear pattern appears, as a function of longitude, in the transports estimated in summer: The mean transport has two maxima, one around 20°W and the other around 15.5°W (Figure 6e), while a mean southward transport is observed between 18.5°W and 17°W, consistent with the mean meridional geostrophic section (Figure 5a) and the mean DAC section (Figure 2b). During winter, there are not enough sections to be able to distinguish clearly a longitudinal structure of the mean transport. Only four sections were carried out west of 19°W, with only one section between 1 January and 31 March (Figure 6f).

Transports are calculated on each section and for each geographical region (Figure 7a). Mean transports are calculated for each region by averaging ϕ_{abs} over all available sections (Table 3). The transport across the whole glider section is calculated as the sum of the mean regional transports. Between 20.6°W and 15°W, the mean transport is 5.1 Sv (standard error of 1.0 Sv) with a standard deviation between sections of 3.2 Sv. During the summer period (May to October), outside the period of subpolar mode water formation, the mean transport between 20.6°W and 15°W is 6.7 Sv (standard error of 0.9 Sv) with a standard deviation between sections of 2.6 Sv.

In summer, the mean flows are higher and the standard deviation between the sections are smaller in the Hatton Bank Jet, the Rockall Bank Jet, and the overall section (Table 3). The mean flows associated with the three branches are (i) 6.3 $\pm$ 2.1 Sv (standard error, *SE*: 0.8 Sv) northward associated with the Hatton Bank Jet

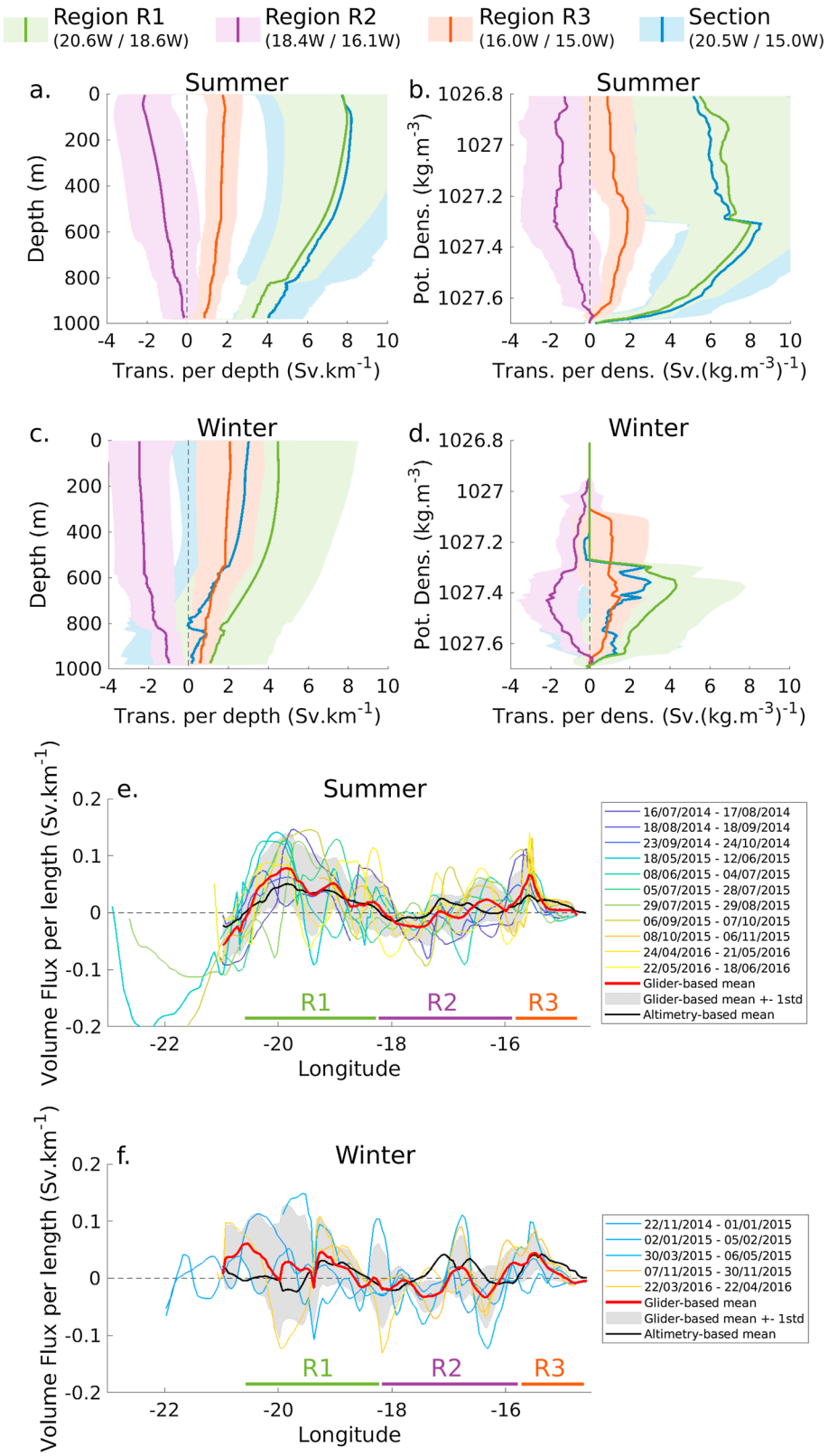

Figure 6. Mean summer (a, b, e) and winter (c, d, f) absolute meridional geostrophic velocity transport by longitude as a function of depth (a, c), density (b, d), and integrated by depth as a function of longitude (e, f). Shaded areas (in panels a–d) correspond to the mean transport ±1 standard deviation for Region R1 (green), Region R2 (purple), Region R3 (orange), and the total section (blue).

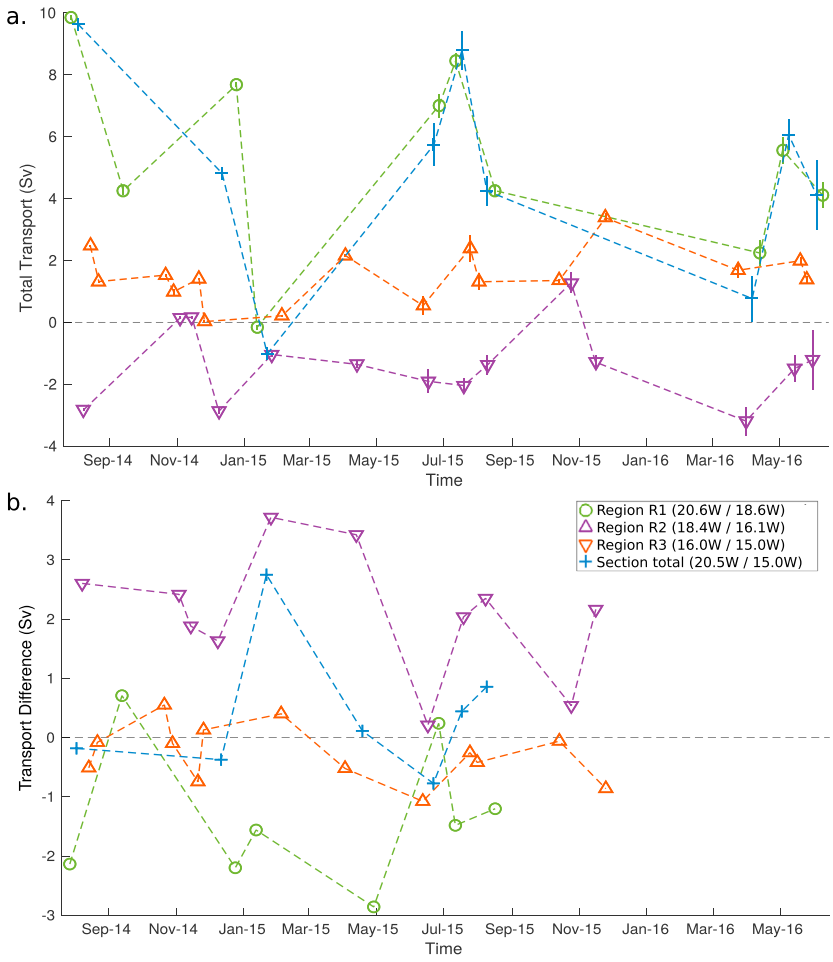

Figure 7. (a) Integrated absolute meridional transport for the layer 0–1,000 m for each glider section along 58°N calculated for regions R1, R2, R3, and the whole section. Uncertainties on individual transport estimated are listed in Table 2 and are indicated by vertical bars. Statistics are summarized in Table 3). (b) Time series of the differences between transport calculated with the altimetry-referenced surface geostrophic velocities and transport calculated with a reference to the glider depth-average current.

(R1), (ii) 1.1 ± 1.4 Sv (SE: 0.5 Sv) southward over the western flank of the HRB (R2, 18.5°W to 16.0°W), and (iii) 1.5 ± 0.7 Sv (SE: 0.2 Sv) northward associated with the Rockall Bank Jet (R3). In winter, the mean flow does not change significantly for the Rockall Bank Jet (1.5 ± 1.2 Sv, SE: 0.5 Sv) but appears 1 Sv stronger in Region R2 (−2.0 ± 1.1 Sv, SE:0.4 Sv) and 3.0 Sv weaker in the Hatton Bank Jet (3.3 ± 3.1 Sv, SE: 1.6 Sv).

The extrema range is greater in the Hatton Bank Jet (R1) compared with the other regions (Table 3). In Region R2 there is no significant difference for the minimum transport (−3.4 Sv in summer and −3.4 Sv in winter). However, the maximum transport appears to be consistently negative in winter (−0.7 Sv), while positive values can be found in summer (maximum of 0.7 Sv). In the Rockall Bank Jet, the extrema range is 1 Sv smaller in summer (min: 0.1 Sv; max: 2.4 Sv) compared with winter (min: 0.2 Sv; max: 3.3 Sv), highlighting a more steady flow in summer. For the overall section, the extrema range is 4 Sv larger during winter (min: −2.0 Sv; max: 5.2 Sv) compared with summer (min: 5.3 Sv; max: 8.9 Sv).

Absolute transport ϕ_{abs} can be separated into depth-independent (named hereafter *barotropic*) ϕ_{bt} and baroclinic parts ϕ_{bc} (equation (6). Transport over the west part of the HRB (Region R2) and in the Rockall Bank Jet is mostly barotropic during summer (mean ratio ϕ_{bc}/ϕ_{abs} of 0.1 and 0.0, Table 4), while in the Hatton Bank Jet, 30% of the absolute transport is due to the vertical geostrophic shear (Table 4).

Table 3
Mean ($\bar{x}$), Standard Deviation (s), Standard Error (SE), Minimum (Min), and Maximum (Max) of the Absolute Meridional Transports (ϕ_{abs}), With the Number of Available Sections (N_{sec})

		ϕ_{abs}					
		$\bar{x}$	s	SE	Min	Max	N_{sec}
Period	Area	(Sv)	(Sv)	(Sv)	(Sv)	(Sv)	
All months	Hatton Bank Jet (20.6°W/18.6°W)	5.1	2.8	0.9	−0.7	9.1	11
	Region R2 (18.4°W/16.1°W)	−1.5	1.3	0.4	−3.4	0.7	14
	Rockall Bank Jet (16.0°W/15.0°W)	1.5	0.9	0.2	0.1	3.3	16
Summer	Hatton Bank Jet (20.6°W/18.6°W)	6.3	2.1	0.8	3.5	9.1	7
	Region R2 (18.4°W/16.1°W)	−1.1	1.4	0.5	−3.4	0.7	7
	Rockall Bank Jet (16.0°W/15.0°W)	1.5	0.7	0.2	0.1	2.4	10
Winter	Hatton Bank Jet (20.6°W/18.6°W)	3.3	3.1	1.6	−0.7	6.4	4
	Region R2 (18.4°W/16.1°W)	−2.0	1.1	0.4	−3.4	−0.7	7
	Rockall Bank Jet (16.0°W/15.0°W)	1.5	1.2	0.5	0.2	3.3	6

Note. Positive (negative) transport values are northward (southward).

$$\underbrace{\iint_{\text{section}} v_n(z)\mathrm{d}x\mathrm{d}z}_{\phi_{\text{abs}}} = \underbrace{\iint_{\text{section}} v_n(-H)\mathrm{d}x\mathrm{d}z}_{\phi_{\text{bt}}} + \underbrace{\iint_{\text{section}} v_{BC}\mathrm{d}x\mathrm{d}z}_{\phi_{\text{bc}}} \tag{6}$$

During winter, all three regions have a high standard error for the mean ratio ϕ_{bc}/ϕ_{abs} (from 0.22 to 1.04) and a high standard deviation between the sections (from 0.58 to 2.08). This highlights the fact that the winter baroclinic transport has a variable contribution, compared with a more *steady* summer period. Ratios for individual sections can be lower than −1 during winter months (see Min in Table 4), indicating a baroclinc transport similar to or larger than the barotropic transport. A possible explanation for this increase in the *baroclinicity* of the flow can be found in the winter intensification of surface buoyancy forcing. Indeed, other studies in regions of water mass formation have shown that surface buoyancy forcing can excite wintertime currents and create a baroclinic shear in the flow (Howard et al., 2015; Lilly et al., 1999).

5. Discussion

5.1. Comparison of the Transport Estimates to Altimetry Data

By analyzing acoustic Doppler current profiler (ADCP) data collected on a repeat section from Greenland to Scotland, Chafik et al. (2014) show that satellite altimetric sea surface height data are in overall good agreement with geostrophically estimated sea level from surface ADCP velocity data. However, they found that altimetric data are unable to resolve mesoscale structures of the topographically defined mean circulation, especially over the Banks Region shown in Figure 1. To quantify the difference involved in using absolute surface geostrophic current from altimetry ($V^{\text{alti}}_{\text{surf}}$) to reference the geostrophic shear in the region of

Table 4
Same as Table 3 But for the Baroclinic Transport ϕ_{bc} and the Ratio ϕ_{bc}/ϕ_{abs}

			ϕ_{bc}					ϕ_{bc}/ϕ_{abs}				
			$\bar{x}$	s	SE	Min	Max	$\bar{x}$	s	SE	Min	Max
Period	Area	N_{sec}	(Sv)	(Sv)	(Sv)	(Sv)	(Sv)	(Sv)	(Sv)	(Sv)	(Sv)	(Sv)
Summer	Hatton Bank Jet	7	2.1	1.3	0.5	0.5	3.9	0.31	0.15	0.06	0.13	0.51
	Region R2	7	−0.2	0.6	0.2	−1.3	0.5	0.11	0.39	0.15	−0.39	0.70
	Rockall Bank Jet	10	0.0	0.3	0.1	−0.4	0.6	−0.04	0.19	0.06	−0.36	0.26
Winter	Hatton Bank Jet	4	2.0	0.6	0.3	1.3	2.8	−0.58	2.08	1.04	−3.69	0.61
	Region R2	7	0.2	0.9	0.3	−0.5	2.0	−0.15	0.58	0.22	−1.36	0.42
	Rockall Bank Jet	6	0.1	0.4	0.1	−0.3	0.7	−0.12	0.65	0.27	−1.37	0.51

our glider study, we calculate absolute geostrophic current referenced to altimetry-derived surface absolute geostrophic current $v_n^{\text{alti}}(z)$, by integrating equation (1) from the depth z to the surface (equation (7)):

$$v_n^{\text{alti}}(z) = V_{\text{surf}}^{\text{alti}} + \frac{g}{\rho_0 f}\int_z^0 \frac{\partial \rho}{\partial s} \mathrm{d}z \tag{7}$$

A longitudinal section of the mean absolute meridional geostrophic velocity referenced to the surface absolute geostrophic current from satellite altimetry is shown in Figure 5c. The differences with the mean absolute geostrophic current derived from the DAC (Figure 5a) may be summarized as follows: (1) a decrease in the velocity in the core of the Hatton Bank Jet (at 19.8°W); (2) a stronger northward flow in the eastern part of Region R2 (17.2°W/16.1°W), leading to less overall southward transport in region R2; (3) a less intensified and broadened core of the Rockall Bank Jet (16.0°W/15.0°W), with a shift of the core from the 1,000-m depth contour in glider observations (Figure 5a) to the 400-m contour in altimetry-based estimate.

By using equation (5) on $v_n^{\text{alti}}(z)$, surface absolute geostrophic currents from altimetry are used to calculate the meridional absolute geostrophic transport $\phi_{\text{abs}}^{\text{alti}}$. The differences with the meridional absolute geostrophic transport estimated from glider DAC $\phi_{\text{abs}}^{\text{gl}}$ are shown in Figure 7b and are summarized in Table 5. A systematic bias can be observed in Region R2 and in the Hatton Bank Jet: the mean difference ($\pm$ 1 standard deviation) $\phi_{\text{abs}}^{\text{alti}} - \phi_{\text{abs}}^{\text{gl}}$ is equal to 2.1 ($\pm$ 1.1) Sv in Region R2 and of −1.1 ($\pm$ 1.1) Sv in the Hatton Bank Jet. This indicates an overestimation of the northward transport in the Western HRB and an underestimation of the transport of the Hatton Bank Jet from the altimetry-based estimate. These regional biases appear to compensate each other, as on the overall section (20.5°W/15.0°W), the mean difference ($\pm$ 1 standard deviation) is equal to 0.4 $\pm$ 1.3 Sv. By looking only in summer, this difference drops to 0.1 $\pm$ 0.8 Sv. The biases are not dependent on the glider mission or on the direction of the glider section (eastward or westward) suggesting that they are related to the delayed time-gridded products, rather than glider observational errors.

Pujol et al. (2016) indicated that geostrophic currents estimated by satellite altimetry are underestimated compared to in situ observations; specifically, they demonstrated that the gridded products are not adapted to resolve the small mesoscale. The comparison with the spectral content computed from full-resolution Saral/AltiKa 1-Hz along-track measurements shows that nearly 60% of the energy observed in along-track measurements at wavelengths ranging from 200 to 65 km is missing in the SLA gridded products. Thus, the small mesoscale current bands in the Hatton-Rockall Basin are not resolved because of the mapping methodology combined with altimeter constellation sampling capability.

5.2. EKE and Variability of the Hatton Bank Jet

The mesoscale variability in the subpolar North Atlantic and the intensity of the eddy activity represented by the EKE has been documented in several studies (e.g., Heywood et al., 1994; Volkov, 2015; White and Heywood 1995). At midlatitudes away from topography, areas of high EKE appear to be associated with areas of energetic currents; therefore, changes in the patterns of EKE can be indicative of changes in the strong current systems (White & Heywood, 1995). Analyses of the EKE field in the subpolar North Atlantic over different periods have shown that regions of high eddy activities are mostly associated with regions of strong currents (Chafik et al., 2014; Hakkinen and Rhines, 2009; Heywood et al. 1994; Reverdin et al. 2003; Volkov, 2015; White and Heywood 1995). We computed the mean surface EKE from satellite altimetry between 2014 and 2016 (Figure 8a) and found similar large-scale patterns as the studies listed above: the highest EKE is located in the Iceland Basin (in the northward extension of the Maury Channel) and in the Rockall Trough.

The presence of cyclonic and anticyclonic eddies has been observed and documented in the Iceland Basin since the 1990s. In July 1991, a cyclonic eddy with a 25-km radius and geostrophic azimuthal current reaching 25 cm/s was detected around 61°N, 20°W during the UK Biogeochemical Ocean Flux (Harris et al., 1997). In summer 1996, an anticyclonic eddy with a 40-km radius and azimuthal speed of 40 cm/s was detected near 59°N, 20°W during the UK Plankton Reactivity in the Marine Environment program (Martin et al. 1998; Wade and Heywood 2001). Another anticyclonic eddy presenting a structure similar to the UK Plankton Reactivity in the Marine Environment eddy was surveyed in June 1998 by Read and Pollard (2001). Zhao, Bower, Yang, Lin, and Zhou (2018) used high-resolution observations to document the structure of an anticyclonic eddy found during the June–November 2015 period in the Iceland Basin (58–59°N, 23–21°W). They also found similar anticyclonic eddies in high-resolution numerical model simulations, which they used to explore eddy formation. It appears that the main generation mechanisms are baroclinic and barotropic instabilities due to

Table 5
Same as Table 3 But for the Mean and RMS Differences in Transport Derived From Glider-Based and Altimetry-Based Absolute Geostrophic Velocity Estimates

			Mean($\phi_{abs}^{glider} - \phi_{abs}^{altimetry}$)					RMS($\phi_{abs}^{glider} - \phi_{abs}^{altimetry}$)				
			$\bar{x}$	s	SE	Min	Max	$\bar{x}$	s	SE	Min	Max
Period	Area	N_{sec}	(Sv)	(Sv)	(Sv)	(Sv)	(Sv)	(Sv)	(Sv)	(Sv)	(Sv)	(Sv)
All months	Hatton Bank Jet	8	−1.3	1.2	0.4	−2.9	0.7	6.3	2.9	1.0	1.8	9.6
	Region R2	11	2.1	1.1	0.3	0.2	3.7	5.8	2.7	0.8	2.7	10.6
	Rockall Bank Jet	13	−0.3	0.5	0.1	−1.1	0.6	1.7	0.6	0.2	0.8	2.6
Summer	Hatton Bank Jet	5	−0.8	1.2	0.5	−2.1	0.7	4.8	2.6	1.2	1.8	8.8
	Region R2	5	1.6	1.1	0.5	0.2	2.6	4.7	2.3	1.0	2.7	8.5
	Rockall Bank Jet	8	−0.2	0.5	0.2	−1.0	0.6	1.9	0.6	0.2	1.2	2.6
Winter	Hatton Bank Jet	3	−2.2	0.7	0.4	−2.9	−1.6	8.8	0.8	0.5	7.9	9.6
	Region R2	6	2.5	0.9	0.4	1.6	3.7	7.0	2.8	1.2	3.7	10.6
	Rockall Bank Jet	5	−0.3	0.6	0.3	−0.9	0.4	1.4	0.7	0.3	0.8	2.4

Note. On each section, differences between the absolute geostrophic velocity referenced to glider depth-average current and that referenced to surface absolute geostrophic current from altimetry are calculated for each grid point (every 3 km). Then the mean and RMS differences are integrated along the section in order to compare these values to the absolute transport estimated across the section (Table 3).

the intensification of the North Atlantic Current over the western slope of the HB. The authors indicate that the westward propagation of these eddies into the central Iceland Basin leads to a superposition of the westward NAC current branch (centered between 24°W and 23°W along 58°N; see Figures 1 and 8a) onto the eddies, yielding asymmetric velocity structure. By examining 23 years of altimetry data, Zhao, Bower, Yang, and Lin (2018) estimate that this type of anticyclonic eddy occupies this region for at least 2 months at a time and a new eddy is generated every few months, leading to a permanent imprint on the long-term mean absolute dynamic topography (ADT) map, centered on 58.5°N, 22°W (Figures 2a and 8a). The authors also found that the presence or absence of this eddy appears to make a significant contribution to the total poleward heat transport variability on time scales from subseasonal to interannual.

The main reason for the higher standard deviation between 21°W and 18°W (Figure 5b) is likely to be due to the meandering of the Hatton Bank Jet associated with the strong mesoscale eddy activity identified by Zhao, Bower, Yang, and Lin (2018). The meridional component of the velocities associated with this anticyclonic eddy centered on 22.5°W can also be seen on the two longest glider sections in June and September 2015 (Figure 4a), but with the northward flowing side of the eddy only partly resolved. Through the instabilities of the NAC, the generation of these anticyclonic eddies along the western slope of the HB will also impact the meridional transport in this region.

Although the west flank of the HB appears to be on average one of the main pathways of the NAC (between 21°W and 19°W, along 58°N; see Figure 1a), the eddy mesoscale activity can potentially deflect the NAC away from the HB flank toward the central Iceland Basin (Figures 8b and 8c). For example, in January 2015, negative transport values on the western flank of the HB (Figure 7a) appear to be associated with a strong eddy activity from 56°N to 59°N centered on 21°W (Figure 8c), which appears to deflect the Hatton Bank Jet in the Iceland Basin. In August 2014, the NAC is crossing 58°N between 21°W and 19°W (Figure 8b); however, large meanders are present above and below 58°N and the Hatton Bank Jet is deflected toward the central Iceland Basinbefore it reaches 59°N. One year later, in August 2015, the pathway of this NAC branch is different: It crosses 58°N between 21°W and 19°W and flows northward along the HB (Figure 8d), as in the 2-year average map (Figure 8a). The deflection of the NAC away from the western flank of the HB, such as in August 2014 and January 2015, appears to be occasional as it cannot be seen in the 2-year average (Figure 8a).

5.3. Spatial Structure of the North Atlantic Current Branches in the Eastern Subpolar Gyre

Our transport estimates along 58°N from 21°W to 15°W are in good agreement with absolute transport estimates from the 2014 and 2016 OSNAP hydrographic cruises. Holliday et al. (2018) computed the absolute northward transport in the upper-layer ($\sigma_0 < 27.50$ kg/m^3), between 21°W and 14°W, finding 6.4 Sv in July 2014 and 5.5 Sv in July 2016. These estimates are very close to our summer mean of 6.7 Sv, calculated in the upper 1,000 m, from 20.5°W to 15°W.

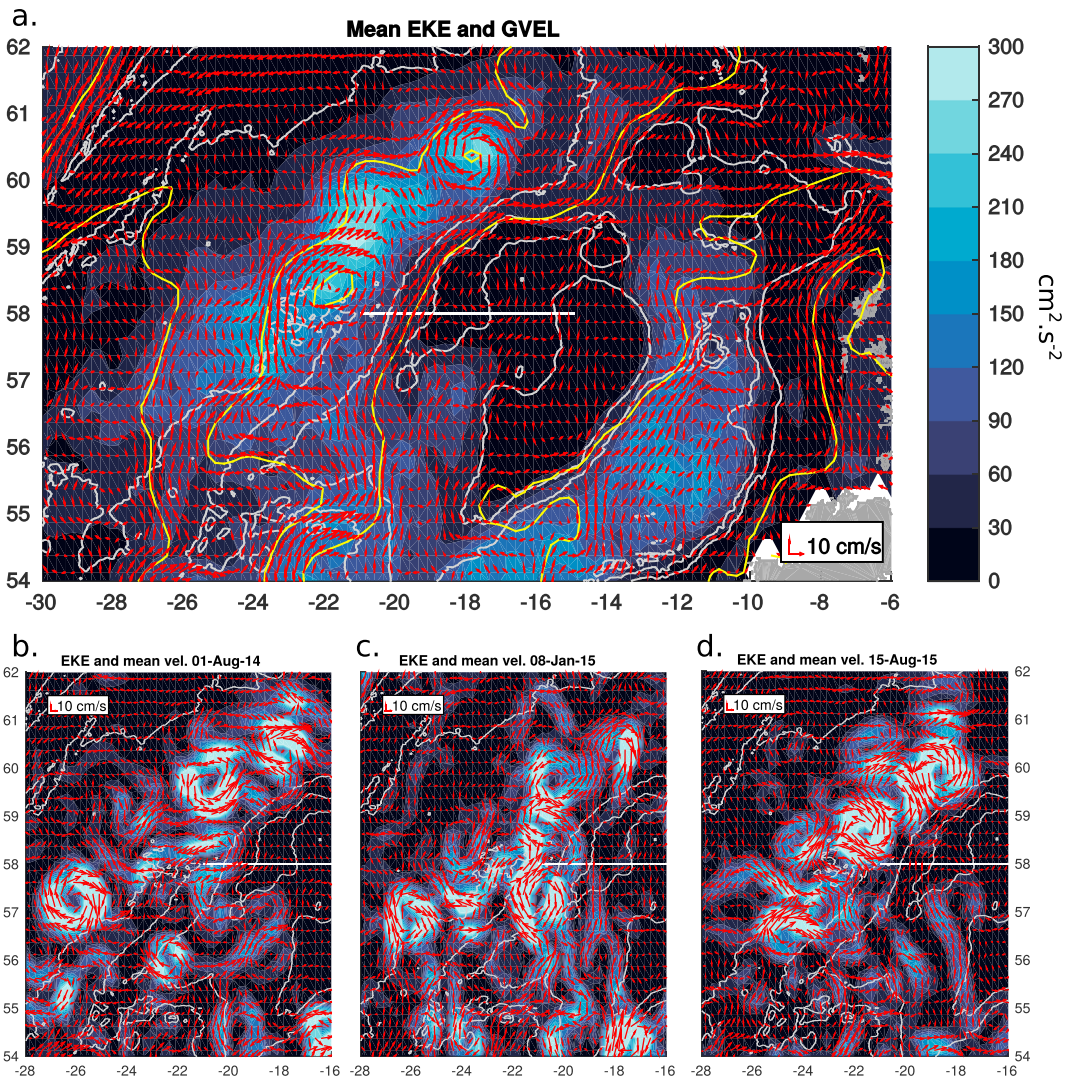

Figure 8. (a) Two-year mean EKE (blue color scale) and surface absolute geostrophic current (red arrows) for the 2014–2015 period, with mean absolute dynamic topography contours plotted in yellow with a contour interval of 0.1 m (labels shown in Figure 9) and 1,000-m bathymetry contours in grey from GEBCO bathymetry. Daily satellite data are shown for 1 August 2014 (b), 8 January 2015 (c), and 15 August 2015 (d). EKE = eddy kinetic energy; GEBCO = General Bathymetric Chart of the Oceans.

Sarafanov et al. (2012) and Rossby et al. (2017) both quantify the meridional transport across 59.5°N using different techniques. Sarafanov et al. (2012) combined 2002–2008 yearly hydrographic measurements with satellite altimetry data and found that 15.5 Sv is transported by the NAC between the Reykjanes Ridge and Scotland (Figure 9), in the upper-layer (σ_0 < 27.55 kg/m^3). Rossby et al. (2017) also found 15.5 Sv along 59.5°N but for a different time period (2012–2016) and using completely different data and a different methodology: They combined measurements of currents from the surface to 700 m from a shipboard ADCP with Argo profiles.

In order to compare their estimates (extending from the Reykjanes Ridge to Scotland) with our results, we used the July 2014 and July 2016 transports computed by Holliday et al. (2018) and take the mean: −2.2 Sv east of the Reykjanes Ridge (−3.2 in 2014 and −1.2 in 2016), 4.3 Sv in the central Iceland (4.0 in 2014 and 4.5 in 2016). In the Rockall Trough, transport estimates were very different between the two years: 7.3 Sv in 2014 and 0.2 Sv in 2016. Although they do present a large variability, certainly due to the high energetic mesoscale recirculation in the Rockall Trough, they do lie within the range estimated from historical temperature and salinity data in the same location (Holliday et al., 2000, 2015). Therefore, we choose to take the long-term

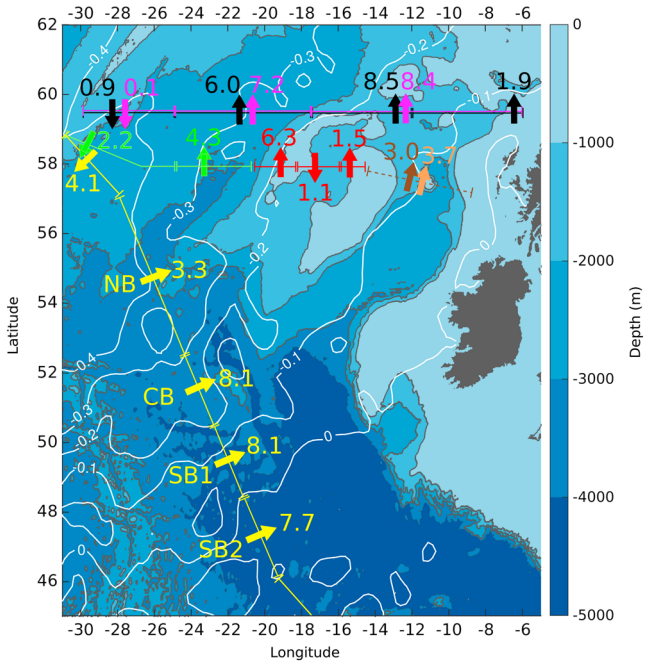

Figure 9. Contours in color from GEBCO bathymetry with the upper-ocean transport calculated from various historical and recent observational data sets. The upper-ocean layer is defined as $\sigma_0 < 27.50$ in Holliday et al. (2018), $\sigma_0 < 27.55$ in Sarafanov et al. (2012) and Rossby et al. (2017), $\sigma_1 < 32.15$ in Daniault et al. (2016), and 1,000 m in the present study. Each colored arrow is perpendicular to a colored line indicating the length of the section used by the different authors for their transport calculation. The position of each arrow corresponds to the position of the velocity maximum on the section. Transport values are expressed in sverdrup and are associated with the 2002–2016 summer mean along the Observatoire de la variabilité interannuelle et décennale en Atlantique Nord (OVIDE) section (yellow arrow; see Daniault et al., 2016), the 2002–2008 summer mean from Sarafanov et al. (2012; black arrows along 59.5°N), the 2012–2016 deseasoned mean from Rossby et al. (2017; pink arrows along 59.5°N), the summer mean of the 2014 and 2016 OSNAP hydrographic sections computed by Holliday et al. (2018; light green arrows between 31°W and 21°W), and the 2014–2016 summer mean calculated in this study (red arrows along 58°N from 21°W and 15°W). In the Rockall Trough, the northward transport in the upper 1,100 m relative to a level of no motion ($\sigma_0 = 27.68$ kg/m^3) is indicated as a brown arrow from Holliday et al. (2015) who calculated it from 11 complete occupations between 1997 and 2014. For the 1975–1998 period, the northward transport above 1,200 m, relative to a level of no motion at 1,200 m, is indicated as an orange arrow (calculated from 24 hydrographic sections; see Holliday et al., 2000). Contours of the mean absolute dynamic topography are plotted in white with a contour interval of 0.1 m. NB = northern branch; CB = central branch; SB = southern branch; GEBCO = General Bathymetric Chart of the Oceans; OSNAP = Overturning in the Subpolar North Atlantic Program.

average value of 3.0 Sv computed by Holliday et al. (2015) from 11 complete occupations between 1997 and 2014 (northward transport in the upper 1,100 m relative to a level of no motion $\sigma_0 = 27.68$ kg/m^3). This value is very close to the 3.7 Sv found by Holliday et al. (2000) from 24 complete occupations during the 1975–1998 period (northward transport above 1,200 m, relative to a level of no motion at 1,200 m). By adding the transports for these different regions along the *OSNAP section*, we find a total of 11.8 Sv which is 3.7 Sv less than Sarafanov et al. (2012) and Rossby et al. (2017) estimates.

South of our glider section, the repeated hydrographic OVIDE (Observatoire de la variabilité interannuelle et décennale en Atlantique Nord) sections were analyzed by Daniault et al. (2016) to compute the 2002–2012 mean summer transport across the section (Figure 9). They identified the signature of NAC branches, which have been reported to cross the Mid-Atlantic Ridge over the Charlie-Gibbs Fracture Zone (northern branch), the Faraday Fracture Zone (central branch), and the Maxwell Fracture Zone (southern branch), shown in Figure 1 (see also Bower & von Appen, 2008; Pollard et al., 2004). The northern and central branches have been reported to head northeastward to the central Iceland Basin, the RP, and the Rockall Trough (Flatau et al., 2003; Hakkinen and Rhines, 2009; Orvik and Niiler, 2002; Pollard et al. 2004). Using time-averaged altimetry-derived velocities, Daniault et al. (2016) found that after crossing the Maxwell Fracture Zone, the southern branch splits into two between the Mid-Atlantic Ridge and the OVIDE section. One branch (SB1) crosses OVIDE at 48.5°N, 21.5°W and continues toward the Rockall Trough and the RP, while the other branch (SB2) crosses OVIDE at 46.1°N, 19.4°W and veers southward in the West European Basin (Figures 1 and 9). The sum of the 2002–2012 mean OVIDE transport in the upper-layer ($\sigma_1 < 32.15$ kg/m^3) for the East Reykjanes Ridge Current (−4.1 Sv), the northern branch (3.3 Sv), the central branch (8.1 Sv), and southern branch SB1 (8.1 Sv) is 15.4 Sv. Remarkably, this number is consistent with the 15.5 Sv calculated by Sarafanov et al. (2012) and Rossby et al. (2017) who computed the transport in the upper-layer ($\sigma_0 < 27.55$ kg/m^3) along 59.5°N, from the Reykjanes Ridge to Scotland (2002–2008 summer mean in Sarafanov et al., 2012; 2012–2016 mean in Rossby et al., 2017).

This good agreement with the 2012–2016 mean calculated by Rossby et al. (2017) led us to formulate the hypothesis that the 2002–2012 summer mean transport calculated across the OVIDE section can also be representative of the 2014–2016 summer mean. Therefore, we then can discuss the NAC transport across the OVIDE section with respect to our results at 58°N. We also computed the mean ADT contours over the 2014–2016 period. The −0.2- and 0-m ADT contours appear to delimit the SB1 branch on the OVIDE section (Figure 9). These contours cross 58°N at 19.5°W and 8°W, suggesting that the 8.1 Sv from the SB1 branch could feed the Rockall Trough and most of the RP, as already discussed by Daniault et al. (2016). The −0.3- and −0.2-m ADT contours delimit the central branch on the OVIDE section, feeding the eastern Iceland Basin (23.5°W to 19.5°W). The 6.3 Sv associated with the Hatton Bank Jet (between 21°W and 18.5°W) is supplied by both the central branch and the southern branch SB1. Interestingly, the horizontal structure of the Hatton Bank Jet meridional velocity presents two cores/branches: one centered on 20°W and another on 19°W (Figure 5a). These two branches are delimited by the −0.2-m ADT contour (crossing the glider section at 19.5°W) which also delimits the central branch and the southern branch SB1 on the OVIDE section.

By adding the mean upper-layer transports computed by Holliday et al. (2018) between 31°W and 21°W with the 2014–2016 mean summer transport from this study, we find an upper-layer transport of 8.8 Sv between 31°W and 15°W. Across OVIDE, the sum of the East Reykjanes Ridge Current with the northern branch and

the central branch correspond to an upper-layer transport of 7.3 Sv toward the Iceland Basin and RP. Therefore, the southern branch SB1 (8.1 Sv) would have to provide the additional 1.5 Sv over the RP. The ADT contours (Figure 9) suggest that the remaining 6.6 Sv would feed the Rockall Trough. Although this estimate is more than twice the mean transport reported previously in the Rockall Trough, it falls within the range of observed transports (Holliday 502 et al., 2000, 2015, 2018) so it is a possible avenue for closing the meridional upper-layer transport between the Reykjanes Ridge and Scotland along 58N. In addition, Sarafanov et al. (2012) found a mean northward transport of 8.5 Sv between 17.5°W and 10°W, with a horizontal structure clearly indicating that most of the northward transport on this section occurs between 15°W and 12°W with the maximum centered on 13°W, in the northward extension of the Rockall Trough.

6. Conclusion

From July 2014 to August 2016, 16 UK-OSNAP glider sections were undertaken over the RP, along 58°N from 21°W to 15°W. The mean absolute geostrophic transport referenced to glider DAC $\pm$ standard deviation is 6.7 $\pm$ 2.6 Sv in summer (May to October), with three main branches (Figure 9): (i) the Hatton Bank Jet, a northward flow of 6.3 $\pm$ 2.1 Sv along the western flank of the Hatton Bank (20.5°W to 18.5°W); (ii) a southward flow of 1.1 $\pm$ 1.4 Sv along the western flank of the Hatton-Rockall Basin (18.5°W to 16.0°W); and (iii) the Rockall Bank Jet, a northward flow of 1.5 $\pm$ 0.7 Sv along the eastern flank of the Hatton-Rockall Basin (16°W to 15°W). On average, these three branches are bathymetrically steered, particularly on the steep slopes of the Hatton and Rockall Banks. The net meridional transport in summer accounts for 43% of the total NAC transport of upper-ocean waters ($\sigma_O < 27.55$) estimated by Sarafanov et al. (2012) and Rossby et al. (2017) along 59.5°N, between the Reykjanes Ridge and Scotland.

With the NAC branches in the Central Iceland Basin and in the Rockall Trough, the Hatton Bank Jet is one of the main NAC pathways in the Eastern Subpolar Gyre. The Hatton Bank Jet appears to be quasi-permanent as it can be seen on both mean absolute surface geostrophic currents from altimetry data and on mean absolute geostrophic sections from repeated glider observations along 58°N. However, it can be occasionally deflected toward the Iceland Basin due to strong mesoscale eddy activity west of the Hatton Bank.

The transport on the western and eastern parts of the Hatton-Rockall Basin is mostly independent of depth during summer, while 30% of the Hatton Bank Jet transport is baroclinic. During winter, transports have a higher variability and geostrophic currents are more baroclinic. The winter intensification of surface buoyancy forcing could be the reason for an enhanced baroclinic shear and winter subpolar mode formation, which may lead to an increase of current variability in the subpolar gyre. More glider sections in winter are needed if one wants to fully characterize and quantify the excitation of wintertime currents by surface buoyancy forcing. Fewer winter observations are available due to logistical difficulties and poor weather conditions, leading to a higher uncertainty on the mean winter meridional transport. However, additional observing efforts are being made to ensure a permanent monitoring of the Hatton Bank Jet in winter.

Comparisons with altimetry-based estimates indicate similar large-scale circulation patterns; however, altimetry data are unable to resolve the small mesoscale current bands in the Hatton-Rockall Basin, which appear to be due to the mapping methodology combined with altimeter constellation sampling capability.

Appendix A: Uncertainty of the Transport Estimates

We used a Monte Carlo approach to assess the uncertainty of transports through individual glider sections. Uncertainties can be due to two components of the geostrophic velocity calculation: the density field and the cross-section component of the DAC. Density is derived from the measurements of conductivity and temperature of the CT sensor manufactured by Sea-bird Scientific and the primary source of uncertainty with this measurement is the drift of the sensor over the course of the glider mission. For each glider section, we create an ensemble of 100 sections of randomly perturbed densities. We add to the original density field a density drift taken from a random uniform distribution for which the boundaries ($\pm$ 0.0025 kg·m^3·month) are determined from the typical stability of the CT sensors (< to 0.001 °C/month in temperature and 0.003/month in salinity, according to Sea-Bird Scientific).

Two main sources of uncertainty can influence the DAC calculation: the accuracy of the surface GPS fixes and the compass calibration. The compass has an accuracy of 1° according to the manufacturer, but magnetic perturbation can invalidate a predeployment calibration of the compass. To tackle this problem, the Seaglider

Table A1
Summary of the True Heading Errors for the Different Glider Missions Determined by all Available On-Land Compass Calibration Checks Carried Out Before or After the Deployment

	OSNAP1		OSNAP2		OSNAP3		OSNAP4		OSNAP5	
Absolute bearing	Err_{port}	Err_{stbd}	Err_{port}	Err_{stbd}	Err_{min}	Err_{max}	Err_{min}	Err_{max}	Err_{port}	Err_{stbd}
30	−0.5	4.0	−13.5	−14.0	−5.0	3.0	−6.0	6.0	−1.5	5.7
60	1.5	4.0	−10.0	−9.0	0	8.0	−6.0	6.0	4.0	7.0
90	3.5	4.0	−3.5	−2.0	−2.0	6.0	−6.0	6.0	7.5	6.0
120	−1.5	−2.0	0.5	2.0	−5.5	2.5	−6.0	6.0	7.5	2.5
150	2.5	0	12.0	14.0	−3.5	4.5	−6.0	6.0	7.0	0
180	−3.0	−6.0	10.5	11.5	−7.0	1.0	−6.0	6.0	4.0	−3.0
210	−1.5	−5.4	4.5	4.5	−11.5	−3.5	−6.0	6.0	2.0	−5.0
240	−1.5	−2.0	2.5	1.0	−11.5	−3.5	−6.0	6.0	−2.0	−5.0
270	−3.5	−4.0	0.5	−1.0	−13.0	−5.0	−6.0	6.0	−4.0	−4.0
300	−2.0	1.0	−2.5	−4.5	−7.0	1.0	−6.0	6.0	−7.0	−3.0
330	−2.0	2.0	−5.0	−6.5	−6.5	1.5	−6.0	6.0	−7.0	0.5
360	−0.5	4.0	−7.0	−7.5	−1.5	6.5	−6.0	6.0	−5.0	4.0
In water calibration		X						X		X
Premission check						X				X
Postmission check		X		X				X		

Note. For four of the five glider deployments, the compass calibration was checked in land (GROOM, 2014), before or after the glider mission. The terms Err_{port} and Err_{stbd} indicate the heading error from compass checks made with different orientations of the glider (turned on port and starboard). For OSNAP3 and OSNAP4, the compass checks for different orientations of the glider was not possible. An Err_{min} and Err_{max} variable is defined for OSNAP3 by using the single-orientation compass check and by adding the maximal difference recorded between a compass check with a starboard orientation and a port orientation (8°). No on-land compass check was available for the OSNAP4 glider mission due to the loss of the glider at the end of the mission. However, an in-flight compass calibration was performed at the beginning of the mission, and thus we determined the heading error as the maximal postmission heading error recorded for a glider which performed an in-flight compass calibration (6°). OSNAP = Overturning in the Subpolar North Atlantic Program.

Fabrication Center developed an in-flight compass calibration, corresponding to a two-dive sequence with two different roll and pitch angles, that allows a compass calibration with in an accuracy a few degrees (Gliders for Research, Ocean Observation and Management [GROOM] 2014). In addition, for four of the five glider deployments, the compass calibration was checked on land (GROOM, 2014), before or after the glider mission. Most of time, the deployment or the recovery of the glider is made from a small coastal boat (where no magnetic disturbance is likely to occur between the on-land compass check and the glider mission). The rest of the time, the glider travels by sea freight and carrier before it is possible to perform an on-land compass check. Thus, we chose the heading errors given by the on-land compass check as being representative of the heading errors of the glider during each mission. The summary of the heading-dependent errors for the different OSNAP missions is shown in Table A1.

The terms Err_{port} and Err_{stbd} indicate the heading error from compass checks made with different orientations of the glider (turned on port and starboard). For OSNAP3 and OSNAP4, the compass checks for different orientations of the glider were not possible. An Err_{min} and Err_{max} variable is defined for OSNAP3 by using the single-orientation compass check and by adding the maximal difference recorded between a compass check with a starboard orientation and a port orientation (8°). No on-land compass check was available for the OSNAP4 glider mission due to the loss of the glider at the end of the mission. However, an in-flight compass calibration was performed at the beginning of the mission; thus, we determined the heading error as the maximum postmission heading error recorded for a glider which performed an in-flight compass calibration (6°).

For each dive, we produced 100 values of heading errors, taken from a random uniform distribution where the boundaries are determined by the on-land compass checks carried out predeployment or postdeployment (variables Err_{port}, Err_{stbd}, Err_{min}, and Err_{max} in Table A1). In addition, we produce for each glider section an ensemble of 100 perturbed start-dive GPS position and end-dive GPS position. We add to the original GPS

positions an error taken from a random exponential distribution, where 95% of the distribution is in a 100-m range (exponential rate of 0.0461; Bennett and Stahr, personal communication, August 2014). For each dive cycle, a perturbed glider heading is created by taking the mean heading of the glider during the dive (calculated from the end-dive dead reckoning position) and by adding to it the random heading error (constant for each glider mission). Then, for each dive, the perturbed start-dive GPS position and the perturbed glider heading are used to recalculate end-dive dead reckoning positions. An ensemble of 100 DAC values is obtained for each dive by calculating the distance between perturbed end-dive dead reckoning position and perturbed end-dive surface GPS position and dividing by the time of the glider dive cycle.

Then these sections of perturbed reference velocities and perturbed densities are used to calculate an ensemble of absolute geostrophic velocities and transport. For each section, our transport estimate corresponds to the mean of the 100 ensemble members and the uncertainty bars are defined as $\pm$ 1 standard deviation between the 100 ensemble members (Figure 7a). Uncertainties calculated for each section are listed in Table 2.

Acknowledgments
We would like to acknowledge the efforts of Karen Wilson and Colin Griffiths in piloting the gliders and assistance from the officers and crew of the R/V *Pelagia* and RRS *Discovery* in recovering the gliders. UK-OSNAP gliders, S. A. C., M. A., and L. H. are supported by the OSNAP NERC Large grant (NE/K010700/1). M. P. is supported by the FASTNEt NERC Consortium grant (NE/I030224/1). C. J. received funding from the European Unions Horizon 2020 research and innovation programme under grant agreement 678760 (ATLAS). S. A. C. was supported by the Blue-Action project (European Union's Horizon 2020 research and innovation programme, grant 727852). S. F. G. was supported by NERC National Capability funding (R8-H12-85). This study has been conducted using E.U. Copernicus Marine Service Information. This output reflects only the authors' view, and the European Union cannot be held responsible for any use that may be made of the information contained therein. BODC curates the near-real-time data set (https://doi.org/10.5285/630bd9f3-2aec-2135-e053-6c86abc01eed). Please see text and references for other data sources. The authors would like to thank Jim Bennett and Fritz Stahr for their support.

References

Bacon, S. (1997). Circulation and fluxes in the North Atlantic between Greenland and Ireland. *Journal of Physical Oceanography*, *27*(7), 1420–1435. https://doi.org/10.1175/1520-0485(1997)027<1420:CAFITN>2.0.CO;2

Bosse, A., Testor, P., Mortier, L., Prieur, L., Taillandier, V., D'Ortenzio, F., & Coppola, L. (2015). Spreading of levantine intermediate waters by submesoscale coherent vortices in the northwestern Mediterranean Sea as observed with gliders. *Journal of Geophysical Research: Oceans*, *120*, 1599–1622. https://doi.org/10.1002/2014JC010263

Bower, A. S., & von Appen, W.-J. (2008). Interannual variability in the pathways of the North Atlantic current over the Mid-Atlantic Ridge and the impact of topography. *Journal of Physical Oceanography*, *38*(1), 104–120. https://doi.org/10.1175/2007JPO3686.1

Boyer, T. P., Antonov, J. I., Baranova, O. K., Coleman, C., Garcia, H. E., Grodsky, A., et al. (2013). World ocean database 2013. In S. Levitus & A. Mishonoc (Eds.), *NOAA atlas* (Vol. 72, p. 209). Silver Spring, MD: NOAA. https://doi.org/10.7289/V5NZ85MT

Brambilla, E., & Talley, L. D. (2008). Subpolar mode water in the northeastern Atlantic: 1. Averaged properties and mean circulation. *Journal of Geophysical Research*, *113*, 1–18. https://doi.org/10.1029/2006JC004062

Buckley, M. W., & Marshall, J. (2016). Observations, inferences, and mechanisms of the Atlantic Meridional Overturning Circulation: A review. *Reviews of Geophysics*, *54*, 5–63. https://doi.org/10.1002/2015RG000493

Chafik, L., Rossby, T., & Schrum, C. (2014). On the spatial structure and temporal variability of poleward transport between Scotland and Greenland. *Journal of Geophysical Research: Oceans*, *119*, 824–841. https://doi.org/10.1002/2013JC009287

Chelton, D. B., DeSzoeke, R. A., Schlax, M. G., El Naggar, K., & Siwertz, N. (1998). Geographical variability of the first baroclinic rossby radius of deformation. *Journal of Physical Oceanography*, *28*(3), 433–460. https://doi.org/10.1175/1520-0485(1998)028<0433:GVOTFB>2.0.CO;2

Daniault, N., Mercier, H., Lherminier, P., Sarafanov, A., Falina, A., Zunino, P., et al. (2016). The northern North Atlantic Ocean mean circulation in the early 21st century. *Progress in Oceanography*, *146*, 142–158. https://doi.org/10.1016/j.pocean.2016.06.007

Egbert, G. D., & Erofeeva, S. Y. (2002). Efficient inverse modeling of barotropic ocean tides. *Journal of Atmospheric and Oceanic Technology*, *19*(2), 183–204. https://doi.org/10.1175/1520-0426(2002)019<0183:EIMOBO>2.0.CO;2

Eriksen, C., Osse, T., Light, R., Wen, T., Lehman, T., Sabin, P., et al. (2001). Seaglider: A long-range autonomous underwater vehicle for oceanographic research. *IEEE Journal of Oceanic Engineering*, *26*(4), 424–436. https://doi.org/10.1109/48.972073

Flatau, M. K., Talley, L., & Niiler, P. P. (2003). The North Atlantic Oscillation, surface current velocities, and SST changes in the subpolar North Atlantic. *Journal of Climate*, *16*(14), 2355–2369. https://doi.org/10.1175/2787.1

Frajka-Williams, E., Eriksen, C. C., Rhines, P. B., & Harcourt, R. R. (2011). Determining vertical water velocities from Seaglider. *Journal of Atmospheric and Oceanic Technology*, *28*(12), 1641–1656. https://doi.org/10.1175/2011JTECHO830.1

Gliders for Research, Ocean Observation and Management (2014). Deliverable 5.3. Report describing best practices for glider missions and sensor use: Preparation, operation, calibration, intercalibration/comparison, and recovery (*Tech. rep.*): European Union—7th Framework Programme.

Hakkinen, S., & Rhines, P. B. (2009). Shifting surface currents in the northern North Atlantic Ocean. *Journal of Geophysical Research*, *114*, C04005. https://doi.org/10.1029/2008JC004883

Hansen, B., Hátún, H., Kristiansen, R., Ølsen, S. M., & sterhus, S. (2010). Stability and forcing of the Iceland-Faroe inflow of water, heat, and salt to the Arctic. *Ocean Science*, *6*(4), 1013–1026. https://doi.org/10.5194/os-6-1013-2010

Harris, R. P., Boyd, P., Harbour, D. S., Head, R. N., Pingree, R. D., & Pomroy, A. J. (1997). Physical, chemical and biological features of a cyclonic eddy in the region of 61.10 N and 19.50 W in the North Atlantic. *Deep Sea Research, Part I*, *44*(11), 1815–1839.

Heywood, K. J., McDonagh, E. L., & White, M. A. (1994). Eddy kinetic energy of the North Atlantic subpolar gyre from satellite altimetry. *Journal of Geophysical Research: Oceans*, *99*(C11), 22,525–22,539. https://doi.org/10.1029/94JC01740

Holliday, N. P., Bacon, S., Cunningham, S., Gary, S. F., Karstensen, J., King, B. A., et al. (2018). Subpolar North Atlantic overturning and gyre-scale circulation in the summers of 2014 and 2016. *Journal of Geophysical Research: Oceans, 123*. https://doi.org/10.1029/2018JC013841

Holliday, N. P., Cunningham, S. A., Johnson, C., Gary, S. F., Griffiths, C., Read, J. F., et al. (2015). Multidecadal variability of potential temperature, salinity, and transport in the eastern subpolar North Atlantic. *Journal of Geophysical Research: Oceans*, *120*, 5945–5967. https://doi.org/10.1002/2015JC010762

Holliday, N., Pollard, R. T., Read, J. F., & Leach, H. (2000). Water mass properties and fluxes in the Rockall Trough, 1975–1998. *Deep Sea Research Part I: Oceanographic Research Papers*, *47*(7), 1303–1332. https://doi.org/10.1016/S0967-0637(99)00109-0

Howard, E., McC. Hogg, A., Waterman, S., Marshall, D. P., Howard, E., Hogg, A. M., et al. (2015). The injection of zonal momentum by buoyancy forcing in a Southern Ocean model. *Journal of Physical Oceanography*, *45*(1), 259–271. https://doi.org/10.1175/JPO-D-14-0098.1

Høydalsvik, F., Mauritzen, C., Orvik, K., LaCasce, J., Lee, C., & Gobat, J. (2013). Transport estimates of the western branch of the Norwegian Atlantic current from glider surveys. *Deep Sea Research Part I: Oceanographic Research Papers*, *79*, 86–95. https://doi.org/10.1016/j.dsr.2013.05.005

Intergovernmental Panel on Climate Change (2014). Climate change 2013—The physical science basis, 1–6. https://doi.org/10.1017/CBO9781107415324

Lee, C. M., & Rudnick, D. L. (2018). Underwater gliders. In R. Venkatesan, A. Tandon, E. D'Asaro, & M. A. Atmanand (Eds.), *Obs. Ocean. Real Time* (pp. 123–139). Cham: Springer Oceanography. Springer International Publishing https://doi.org/10.1007/978-3-319-66493-4

Liblik, T., Karstensen, J., Testor, P., Alenius, P., Hayes, D., Ruiz, S., et al. (2016). Potential for an underwater glider component as part of the Global Ocean Observing System. *Methods in Oceanography*, *17*, 50–82. https://doi.org/10.1016/j.mio.2016.05.001

Lilly, J. M., Rhines, P. B., Visbeck, M., Davis, R., Lazier, J. R. N., Schott, F., & Farmer, D. (1999). Observing deep convection in the Labrador Sea during winter 1994/95. *Journal of Physical Oceanography*, *29*(8), 2065–2098. https://doi.org/10.1175/1520-0485(1999)029<2065:ODCITL>2.0.CO;2

Lozier, M. S., Bacon, S., Bower, A. S., Cunningham, S. A., Femke de Jong, M., de Steur, L., et al. (2017). Overturning in the Subpolar North Atlantic Program: A new international ocean observing system. *Bulletin of the American Meteorological Society*, *98*(4), 737–752. https://doi.org/10.1175/BAMS-D-16-0057.1

Martin, A. P., Wade, I. P., Richards, K. J., & Heywood, K. J. (1998). The PRIME eddy. *Journal of Marine Research*, *56*(2), 439–462. https://doi.org/10.1357/002224098321822375

Orvik, K. A., & Niiler, P. (2002). Major pathways of Atlantic water in the northern North Atlantic and Nordic Seas toward Arctic. *Geophysical Research Letters*, *29*(19), 2–1–2–4. https://doi.org/10.1029/2002GL015002

Pelland, N. a., Eriksen, C. C., & Lee, C. M. (2013). Subthermocline eddies over the Washington continental slope as observed by seagliders, 200309. *Journal of Physical Oceanography*, *43*(10), 2025–2053. https://doi.org/10.1175/JPO-D-12-086.1

Pollard, R. T., Read, J. F., Holliday, N. P., & Leach, H. (2004). Water masses and circulation pathways through the Iceland basin during Vivaldi 1996. *Journal of Geophysical Research*, *109*, 1–10. https://doi.org/10.1029/2003JC002067

Pujol, M. I., Faugère, Y., Taburet, G., Dupuy, S., Pelloquin, C., Ablain, M., et al. (2016). DUACS DT2014: The new multi-mission altimeter data set reprocessed over 20 years. *Ocean Science*, *12*(5), 1067–1090. https://doi.org/10.5194/os-12-1067-2016

Read, J. F., & Pollard, R. T. (2001). A long-lived eddy in the Iceland Basin 1998. *Journal of Geophysical Research*, *106*(C6), 11,411–11,421. https://doi.org/10.1029/2000JC000492

Reverdin, G., Niiler, P. P., & Valdimarsson, H. (2003). North Atlantic Ocean surface currents. *Journal of Geophysical Research*, *108*(C1), 2–21. https://doi.org/10.1029/2001JC001020

Rhines, P., Häkkinen, S., & Josey, S. A. (2008). *Arctic Subarctic Ocean Fluxes* (pp. 87–109). Dordrecht: Springer Netherlands. https://doi.org/10.1007/978-1-4020-6774-7

Rossby, T., & Flagg, C. N. (2012). Direct measurement of volume flux in the Faroe-Shetland Channel and over the Iceland-Faroe Ridge. *Geophysical Research Letters*, *39*. https://doi.org/10.1029/2012GL051269

Rossby, T., Reverdin, G., Chafik, L., & Søiland, H. (2017). A direct estimate of poleward volume, heat, and freshwater fluxes at 59.5N between Greenland and Scotland. *Journal of Geophysical Research: Oceans*, *122*, 5870–5887. https://doi.org/10.1002/2017JC012835

Rudnick, D. L. (2016). Ocean research enabled by underwater gliders. *Annual Review of Marine Science*, *8*(1), 519–541. https://doi.org/10.1146/annurev-marine-122414-033913

Rudnick, D. L., & Cole, S. T. (2011). On sampling the ocean using underwater gliders. *Journal of Geophysical Research*, *116*, C08010. https://doi.org/10.1029/2010JC006849

Sarafanov, A., Falina, A., Mercier, H., Sokov, A., Lherminier, P., Gourcuff, C., et al. (2012). Mean full-depth summer circulation and transports at the northern periphery of the Atlantic Ocean in the 2000s. *Journal of Geophysical Research*, *117*. https://doi.org/10.1029/2011JC007572

Serreze, M. C., Holland, M. M., & Stroeve, J. (2007). Perspectives on the Arctic's shrinking sea-ice cover. *Science*, *315*(5818), 1533–1536. https://doi.org/10.1126/science.1139426

Smith, D. M., Eade, R., Dunstone, N. J., Fereday, D., Murphy, J. M., Pohlmann, H., & Scaife, A. A. (2010). Skilful multi-year predictions of Atlantic hurricane frequency. *Nature Geoscience*, *3*(12), 846–849. https://doi.org/10.1038/ngeo1004

Straneo, F., Hamilton, G. S., Sutherland, D. A., Stearns, L. a., Davidson, F., Hammill, M. O., et al. (2010). Rapid circulation of warm subtropical waters in a major glacial fjord in East Greenland. *Nature Geoscience*, *3*(3), 182–186. https://doi.org/10.1038/ngeo764

Sutton, R. T. (2005). Atlantic ocean forcing of North American and European summer climate. *Science (80-.)*, *309*(5731), 115–118. https://doi.org/10.1126/science.1109496

Testor, P., Meyers, G., Pattiaratchi, C., Bachmayer, R., Hayes, D., Pouliquen, S., et al. (2010). Gliders as a component of future observing systems. In J. Hall, D. E. Harrison, & D. Stammer (Eds.), *Proc. OceanObs'09 Sustain. Ocean Obs. Inf. Soc.* (Vol. *2*, pp. 961–978). OceanObs'09, Venice, Italy: ESA Publication. https://doi.org/10.5270/OceanObs09.cwp.89

Todd, R. E., Rudnick, D. L., & Davis, R. E. (2009). Monitoring the greater San Pedro Bay region using autonomous underwater gliders during fall of 2006. *Journal of Geophysical Research*, *114*, C06001. https://doi.org/10.1029/2008JC005086

Todd, R. E., Rudnick, D. L., Mazloff, M. R., Davis, R. E., & Cornuelle, B. D. (2011). Poleward flows in the Southern California current system: Glider observations and numerical simulation. *Journal of Geophysical Research*, *116*, 1–16. https://doi.org/10.1029/2010JC006536

Trenberth, K. E., Large, W. G., & Olson, J. G. (1990). The mean annual cycle in global ocean wind stress. *Journal of Physical Oceanography*, *20*(11), 1742–1760. https://doi.org/10.1175/1520-0485(1990)020<1742:TMACIG>2.0.CO;2

University of Washington (2016). Seaglider quality control manual for basestation 2.09 (*Tech. rep.*) University of Washington: School of Oceanography and Applied Physics Laboratory.

Volkov, D. L. (2015). Eddy field and its spatial and temporal variability in the North Atlantic Ocean as observed with satellite altimetry: Interannual variability of the altimetry-derived eddy field and surface circulation in, (April 2003).

Wade, I. P., & Heywood, K. J. (2001). Tracking the PRIME eddy using satellite altimetry. *Deep Sea Research Part II: Topical Studies in Oceanography*, *48*(4-5), 725–737. https://doi.org/10.1016/S0967-0645(00)00094-1

White, M. A., & Heywood, K. J. (1995). Seasonal and interannual changes in the North Atlantic subpolar gyre from Geosat and TOPEX/POSEIDON altimetry. *Journal of Geophysical Research*, *100*(C12), 24,931–24,941. https://doi.org/10.1029/95JC02123

Xu, W., Miller, P. I., Quartly, G. D., & Pingree, R. D. (2015). Seasonality and interannual variability of the European slope current from 20 years of altimeter data compared with in situ measurements. *Remote Sensing of Environment*, *162*, 196–207. https://doi.org/10.1016/j.rse.2015.02.008

Zhang, R., & Delworth, T. L. (2006). Impact of Atlantic multidecadal oscillations on India/Sahel rainfall and Atlantic hurricanes. *Geophysical Research Letters*, *33*, L17712. https://doi.org/10.1029/2006GL026267

Zhao, J., Bower, A., Yang, J., & Lin, X. (2018). Meridional heat transport variability induced by mesoscale processes in the subpolar North Atlantic. *Nature Communications*, *9*(1), 1–9. https://doi.org/10.1038/s41467-018-03134-x

Zhao, J., Bower, A. S., Yang, J., Lin, X., & Zhou, C. (2018). Structure and formation of anticyclonic Eddies in the Iceland basin. *Journal of Geophysical Research: Oceans, 123*. https://doi.org/10.1029/2018JC013886